CONTROL SYSTEM DESIGN OF A HIGHLY-EXTENSIBLE SOFT CONTINUUM ROBOT

by

Şeref Kemal Talaş

B.S., Mechanical Engineering, Boğaziçi University, 2016

Submitted to the Institute for Graduate Studies in
Science and Engineering in partial fulfillment of
the requirements for the degree of
Master of Science

Graduate Program in Mechanical Engineering
Boğaziçi University

2019

ACKNOWLEDGEMENTS

First of all, I would like to thank my thesis supervisor Prof. Evren Samur for his patient guidance during my master study. He not only guided my research but also tried to improve my academic skills and prepared me for my future academic studies. I would also like to thank Prof. Çetin Yılmaz and Prof. Onur Özcan for accepting to be jury members of my thesis and for their time.

I sincerely thank all of my friends in RoboCol project, including Timur Altınsoy, Bora Baydere and Cem Tutcu for their collaboration with the mechanical design and Onur Mert Erkan for his contributions to design of the user interface and control system. I am grateful to my friends Taylan, Burcu, Serhat, Uğur and Günay in Haptics and Robotics lab for their support and company. I would like to give my special thanks to my beloved friend Kübra Karacan for her contribution to the position controller tests, and her support and friendship before and during my master study. I would also like to thank Günay Turan for his guidance with the electronics.

Finally, I would like to thank my father Namık, and my mother Sevinç for their precious love and support.

This project is supported by the Scientific and Technological Research Council of Turkey (TÜBİTAK #115E717).

ABSTRACT

CONTROL SYSTEM DESIGN OF A HIGHLY-EXTENSIBLE SOFT CONTINUUM ROBOT

In this thesis, control system design of a highly-extensible soft robot is presented. The robot is actuated with three inflatable tubings connected to stepper motors and can move in three-dimensional space. Pressurizing the tubings provides the body stiffness and creates a thrust at the end-effector to move the robot, whereas position and speed of the tubings are controlled by the stepper motors. Control system includes open-loop speed and position controllers. Also, a teleoperation controller is designed to move the robot by user input from a commanding device. The speed controller is designed only for straight extension and contraction, and it does not provide a three-dimensional speed control. The position controller moves the robot tip to the desired real-world coordinates in three-dimensional space. Finally, the teleoperation controller is used to control the extension/contraction speed and to steer the robot by differentiating the speed of three tubings depending on the user input. The robot is subjected to tests in free-space to measure the accuracy of the speed and position controllers. The teleoperation controller is also tested using the commanding device in order to check whether it is possible to move the robot tip to a target in free-space, through obstacles, and in an enclosed environment. All of the controllers are validated by the experiments. Considering the test results, the proposed highly-extensible soft continuum robot and the designed controllers are promising for many applications such as inspection, urban search and rescue, and minimally invasive surgery.

ÖZET

YÜKSEK MİKTARDA UZAYABİLEN BİR YUMUŞAK ROBOTUN KONTROL SİSTEMİ TASARIMI

Bu tezde yüksek miktarda uzayabilen bir yumuşak robotun kontrol sistemi sunulmuştur. Bahsedilen robot step motorlara bağlanmış üç adet şişebilen boru ile tahrik edilmiş olup, üç boyutlu uzayda hareket edebilmektedir. Basınç sistemi boruların şişirilmesi ile robotun gövde katılığını ve uç elemanındaki tahrik kuvvetini sağlarken, step motorlar robotun hareket hızı ve yönünü belirlemekte kullanılmıştır. Tasarlanan kontrol sistemi, açık döngü hız ve pozisyon kontrolcüleri ile birlikte kumanda yardımıyla robotu yönlendiren bir uzaktan yönetim kontrolcüsünü de barındırmaktadır. Hız kontrolcüsü yalnızca düz uzama ve kısalma için tasarlanmış olup, üç boyutlu uzayda hız kontrolü sağlamamaktadır. Pozisyon kontrolcüsü robotun uç elemanını sıfır konumundan üç boyutlu uzaydaki istenilen koordinatlara hareket ettirmek için tasarlanmıştır. Son olarak, uzaktan yönetim kontrolcüsü, kumanda cihaz aracılığıyla, robotun hızı ve dönme yönünü kontrol etmek amacıyla tasarlanmıştır. Hız ve pozisyon kontrolcülerinin hassasiyetini değerlendirmek amacıyla, robot serbest uzayda belirli testlere tabi tutulmuştur. Uzaktan yönetim kontrolcüsü ise robotu serbest uzayda, engeller arasından ve etrafı kapalı alanda belirlenen hedefe yönlendirmek amacıyla test edilmiştir. Yapılan deneyler tüm kontrolcülerin doğruluğunu onaylamıştır. Test sonuçları göz önüne alındığında, sunulan yumuşak robot ve kontrolcülerinin inceleme, arama kurtarma ve laparoskopik cerrahi gibi alanlarda umut vadettiği söylenebilir.

TABLE OF CONTENTS

LIST OF FIGURES

LIST OF TABLES

LIST OF SYMBOLS

A_{pt}	Filtered analog output of pressure transmitter in mA
I_b	Base current of the transistor in mA
I_c	Collector current of the transistor in mA
I_e	Emitter current of the transistor in mA
I_v	Operating current of the solenoid valves in mA
P	Pressure of the tubings in kPa
p_x	Position output of omega.6 in longitudinal axis in mm
R	Radius of curvature of the robot backbone
R_b	Base resistance of the transistor circuit in Ω
r_{sp}	Radius of the spools in mm
S_b	Backbone length of the robot in mm
S_i	Length of tubing i in mm
T_m	Period of motor control loop in μs
V_b	Base voltage of the transistor circuit in V
V_c	Collector voltage of the transistor circuit in V
v_{ee}	Velocity of the end-effector in mm/s
v_{max}	User input for maximum velocity of the end-effector in mm/s
v_{min}	User input for minimum velocity of the end-effector in mm/s
v_{test}	Position test speed inputted by user in mm/s
V_v	Operating voltage of the solenoid valves in V
W_v	Power of the solenoid valves in watt
x	Axis of fixed frame of the robot
x'	Axis of relative frame of the end-effector
y	Axis of fixed frame of the robot
y'	Axis of relative frame of the end-effector
z	Axis of fixed frame of the robot
z'	Axis of relative frame of the end-effector

α	Orientation output of omega.6 in degrees
β	Orientation output of omega.6 in degrees
β_t	DC current gain of transistor
γ	Angle between z'-axis and the straight line between origin and goal point
η	Step resolution of the stepper motors
Θ_i	Position of the motor i in step
θ_i	Position of the motor i in rad
κ	Curvature of the robot backbone
ϕ	Rotation angle with respect to the fixed frame y axis
ω_i	Rotational speed of the motor i in rpm
ω_{slow}	Speed of the slower motor during rotation in rpm
ω_{test}	Translational test speed converted to rotational motor speed in rpm

LIST OF ACRONYMS/ABBREVIATIONS

2D	Two dimensional
3D	Three dimensional
ACU	Air control unit
ADC	Analog to digital converter
AI	Analog Input
AO	Analog Output
BHA	Bionic handling assistant
CC	Constant curvature
cRIO	CompactRIO Real-Time Controller
DI	Digital Input
DIO	Digital Input-Output
DO	Digital Output
DoF	Degree-of-freedom
FEM	Finite element method
FPGA	Field programmable gate arrays
FU	Feed unit
GUI	Graphical user interface
NI	National Instruments
NPN	Negative-positive-negative
PAMs	Pneumatic artificial muscles
PWM	Pulse width modulation
RMSE	Root-mean-square error
RTOS	Real-Time operating system
SDK	Software development kit
SMC	Sliding-mode controller
sPAM	Series pneumatic artificial muscle
SPAs	Soft pneumatic actuators

1. INTRODUCTION

Continuum robots are defined such that their number of links approaches to infinity and link lengths approach to zero [1]. Their movement is a combination of continuous arcs formed by each actuatable section. This type of robots are usually bio-inspired robots, because the idea behind them is originated from snakes, elephant trunks, climbing plants etc. For the last 10 years, bio-inspiration led the research to the robots made of soft materials to increase dexterity of continuum robots by adopting the compliance of their biological analogues.

As soft materials replaced the rigid links or joints of the robots, the soft robot concept emerged and conventional robots are started to be called rigid or hard robots as shown in Figure 1.1. Various definitions are given to soft robots depending on the material, structural geometry, and locomotion methods since it is a very recent subject of research. The most acknowledged definition by the research community around the world is given by Cianchetti *et. al.* [2] as follows: "soft robots/devices that can actively interact with the environment and can undergo "large" deformations relying on inherent or structural compliance".

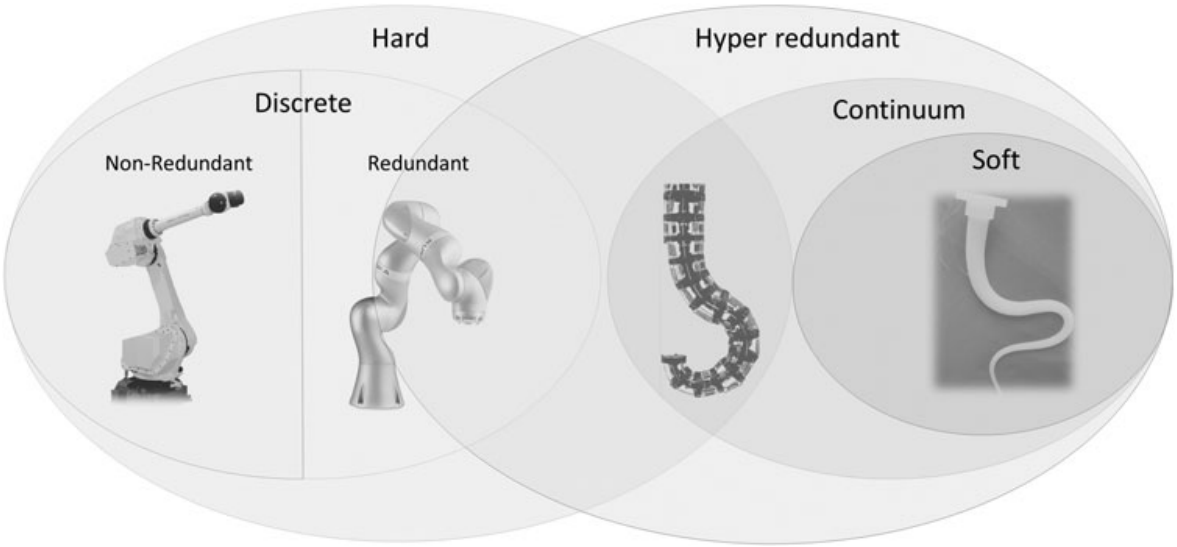

Figure 1.1. Categorization of robots, from rigid to soft [3].

Soft robots introduce new challenges in modeling and control [4]. Even though there are some methods adopted from the conventional approaches [5], they require different control approaches than rigid robots due to the following reasons: They do not have finite number of joints with limited degrees-of-freedom (DoF) as rigid robots, they undergo elastic deformation during motion, and they are made of materials with nonlinear characteristics [3]. Another challenge in control is lack of feedback from the robot (i.e., position, orientation, force). Therefore, most soft robots have open-loop control systems. Although there are certain modeling methods and control systems defined depending on actuation type, each continuum robot needs a novel control system as well, because of the wide spectrum of design and actuation methods used for soft and/or continuum robots [3]. In this study, a control system design is introduced for a novel pneumatic soft-continuum robot which is developed in a parallel study by Baydere [6].

1.1. Aim of the Study

The aim of this study is to develop a control system for a novel pneumatic soft robot that can move in 3D space. The robot requires a novel control system since the actuation method is original compared to other pneumatic robots as the tubing pressure and robot speed are decoupled. The control system include mechatronic components as well as a speed controller for straight extension/contraction, a position controller for movement in free space, and a teleoperation controller for navigation of the robot.

2. LITERATURE REVIEW

Soft continuum robots have been an emerging research topic for the last 10 years. They offer increased navigation and manipulation capabilities in convoluted, and cluttered environments because of their ability to conform to their surroundings (see Figure 2.1). They can be built at smaller scales, and cost lower than rigid robots. Soft robots resolve the most prominent problem of rigid robots which is unsafe human-robot interaction. They undergo high deformations to absorb energy providing safer interaction [7]. Researchers have successfully developed soft continuum robots inspired from biology such as tentacles [8–10], snakes [11, 12], and climbing plants [13, 14] for a variety of applications including minimally invasive surgery [15, 16], urban search and rescue [17], and inspection [14, 18]. In this chapter, relative literature about actuation, modeling, and control methods of soft robots are given.

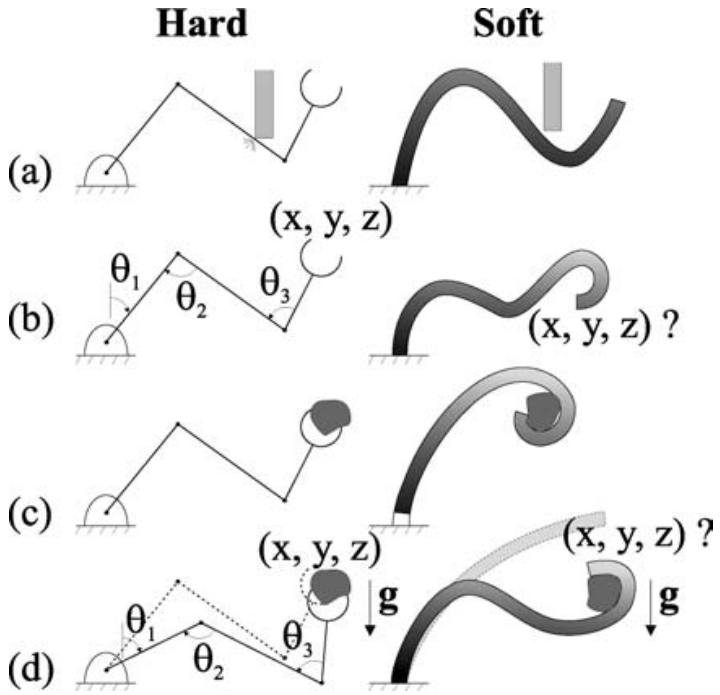

Figure 2.1. Capabilities of hard and soft robots: (a) dexterity, (b) position sensing, (c) manipulation and (d) loading [19].

2.1. Actuation Methods

Depending on the place of actuation, soft continuum robots are actuated either intrinsicly or extrinsicly. Intrinsic actuation is performed within the main body, whereas extrinsic actuation is from outside of the body using some mechanical transmission [20]. Extrinsic actuation systems are usually tendons driving the sections to get the desired curvature or concentric tubes with predefined shape, driven from the base of the structure. The most common type of extrinsicly actuators are tendon drive systems. They consist of four tendons attached to the tips of sections of the robot [21]. The reciprocal tendons act in opposite manner since a tendon can only provide tension, e.g. while one tendon is extending, its reciprocal contracts.

Intrinsic actuators such as hydraulic chambers, pneumatic chambers, shape memory alloys or elastomers, fiber-reinforced elastomers and pneumatic artificial muscles are more commonly used than extrinsic actuators [15]. Soft pneumatic actuators (SPAs) are widely used in soft robotics because of their ease of manufacturing, low cost and weight [22]. Pneumatic Artificial Muscles (PAMs) are the most common type of SPAs. Their structure consists of inflatable core covered with fiber braided in a way that it contracts when pressurized [23]. Recent designs offer using multiple PAMs attached in series which are called Series Pneumatic Artificial Muscle (sPAM) [24].

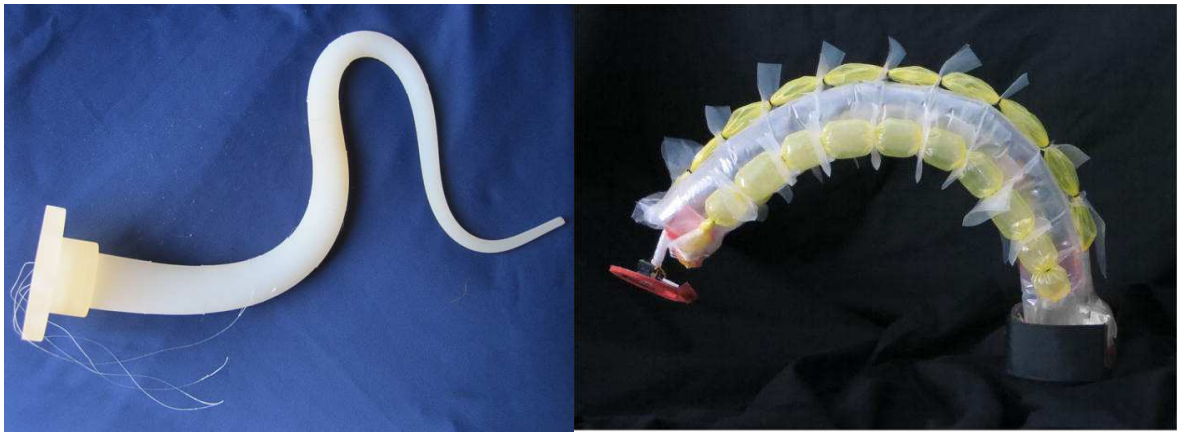

Figure 2.2. Tendon driven octopus arm-like robot (left) [21], soft robot actuated by sPAM (right) [24].

2.2. Modeling Methods

Constant curvature modeling approaches that are used for continuum robots are commonly used in modeling of soft robots [25–27]. These models are mostly focused on quasi-static kinematics, because the dynamics are usually neglected. The reasons of neglecting dynamics are that these robots are slender with low mass which results in higher modal frequencies than the frequencies of their motion, and the effects of inertia are insignificant because the actuator forces absorbed by elastic deformation or friction since they usually move while interacting with the environment rather than in free space [15]. Recent studies present piece-wise constant curvature methods for kinematic and dynamic modeling of soft robots [28, 29]. Also, some conventional methods used in rigid link robots such as D-H parameters or Frenet-Serret frames are also used for homogeneous transformation in some studies after the shape is modeled with continuum robot models [30, 31].

2.3. Control Methods

As the new materials and actuation methods are developed for soft robots, continuum robot models became insufficient to approximate the Jacobian matrices, especially due to high strain deformations caused by environmental interaction [32]. Making use of the environmental interaction, new control methods are developed for soft robots [22]. The controllers used in soft robots can be classified in three main categories, which are (1) model-based controllers, (2) model-free controllers, and (3) hybrid controllers [3]. Some of the recent studies on soft robot controllers for most common actuators are given in Table 2.1.

2.3.1. Model-based Controllers

Renda *et. al.* [21] designed a steady-state controller for single piece octopus-like tendon driven soft robot by modeling the exact geometric shape of the robot body. They modeled the robot as a slender Cosserat beam which is a combination of one-dimensional infinitesimal rigid bodies defined by a global position vector and a local

Table 2.1. Recent studies on controllers for pneumatic and tendon driven soft robots.

	Model-based	**Model-free**	**Hybrid**
Tendon Driven	Renda *et. al.* [21] Largilliere *et. al.* [34] Qi *et. al.* [36]	Giorelli *et. al.* [33] Thuruthel *et. al.* [35] Yip *et. al.* [32]	—
Pneumatic	Mahl *et. al.* [37] Kapadia *et. al.* [40] Falkenhahn *et. al.* [43]	Melingui *et. al.* [38] Rolf *et. al.* [41]	Lakhal *et. al.* [39] Reinhart *et. al.* [42]

coordinate frame. They adopted the classical beam theory by neglecting shear strains, and using two bendings, torsion and longitudinal strain values to obtain geometric transformation between consecutive bodies, thus, reconstructed the shape of the body.

Largilliere *et. al.* [34] proposed an inverse kinematic model for soft robots, obtained from Finite Element Method (FEM) which is then solved by using a quadratic programming algorithm. While FEM can model the deformation of soft robots accurately, it is not compatible for real-time control due to computational cost. Therefore, they also proposed a multi-rate controller to run the FEM calculations on a low rate loop while controlling the robot in another loop with high rate. They used a shared buffer to communicate the two asynchronous loops, in order to send the calculated control parameters (tendon lengths) to the control loop while receiving the constraint values, e.g. end-effector position, from control loop as shown in Figure 2.3. They validated the controller on a tendon driven soft robot, calculating the inverse kinematics with 600 Hz frequency. Even though they obtained a control frequency higher than other controllers in literature, this value may be lower for other soft robots depending on the complexity of robot body and actuation method.

The most common intrinsic actuators used in soft robots are pneumatic actuators. Mahl *et. al.* [37] developed a kinematic controller based on a variable curvature model for multi-section pneumatic soft robots . The proposed variable curvature model is a

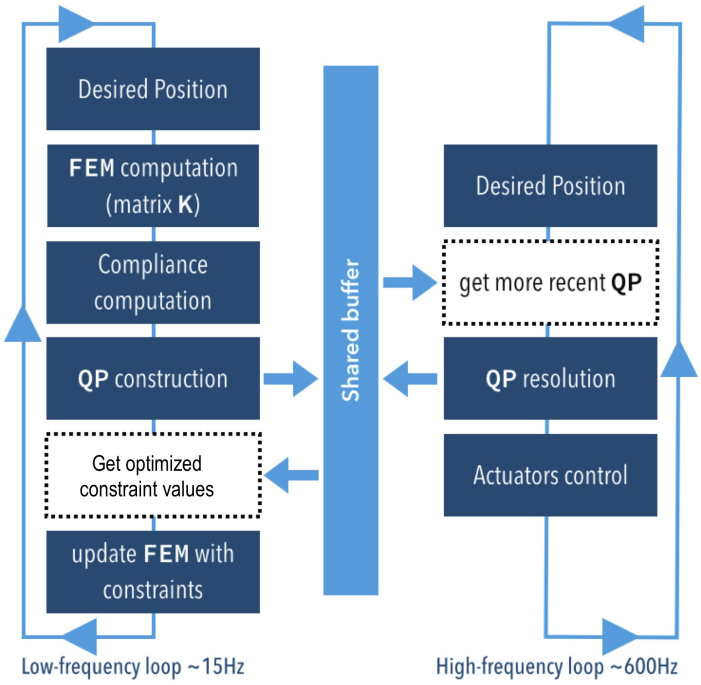

Figure 2.3. Multi-rate control algorithm combining low frequency FEM computation and high frequency robot control algorithm [34].

combination of finite number of serially connected circular arcs with different constant curvature (CC) parameters, therefore, the model is piecewise CC. They used a first order resolved rate algorithm to solve the redundant inverse kinematics and experimentally validated the controller on the Bionic Handling Assistant (BHA) which is a trunk-like manipulator designed by Festo Inc., which is built of three serially connected sections, each actuated by three pneumatic actuators. This controller is applicable for all continuum robots with finite number of serially connected sections that has 3-DoFs which are two bendings and one extension.

Kapadia *et. al.* [40] proposed a planar nonlinear sliding-mode controller (SMC) for an extensible pneumatic soft robot called the OctArm. The robot consists of three serially attached sections, each having three McKibben actuators. The robot is kinematically redundant since it has 9-DoF in 2D space. They used a CC approach for kinematic model, using length, curvature and orientation of each section as configuration space parameters to decide the end-effector position. They used string encoders

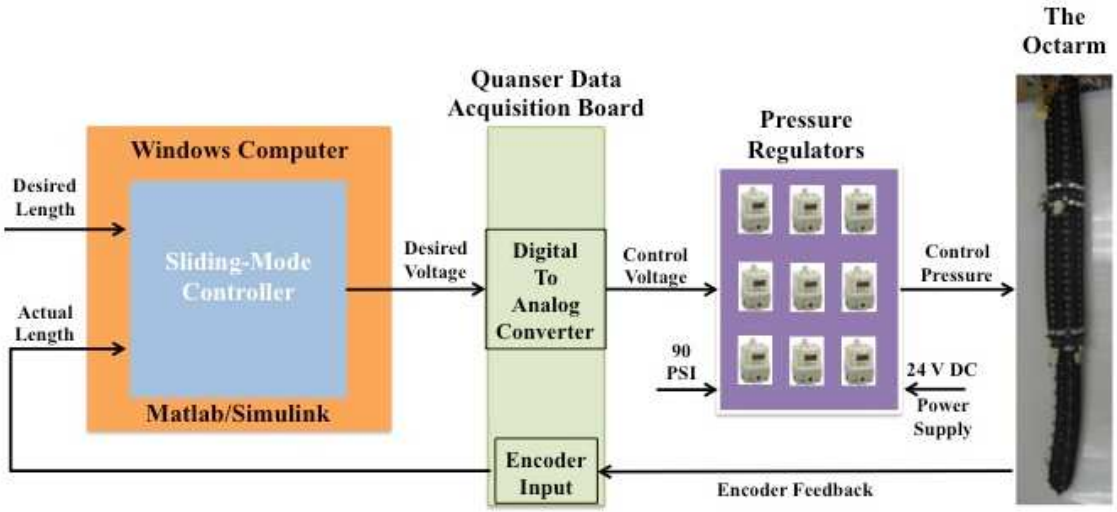

Figure 2.4. Control schematic of sliding-mode controller of OctArm [40].

to measure the section lengths for closed-loop control as shown in Figure 2.4. They validated the SMC to control the tip position of the redundant robot, using a non-redundant rigid-link master robot. They also compared the controller with a PD controller to confirm the effectiveness of SMC over standard controllers. This controller is applicable for planar extensible manipulators, and not applicable for 3D control.

Falkenhahn *et. al.* [43] developed a model-based dynamic controller for BHA. They modeled each actuator as a spring-damper-mass system, where the actuation force created by chamber pressure works against spring and damper forces. They altered the actuator model to obtain a section model including interconnections of parallel actuators, since each actuator acts as external disturbance to the others. They decoupled the pressure and actuator length controllers. They used feedback linearization for pressure control to compensate pneumatic nonlinearities, and a combination of linear PD and feedforward controllers for actuator length control. Therefore, they obtained a cascaded control system as shown in Figure 2.5.

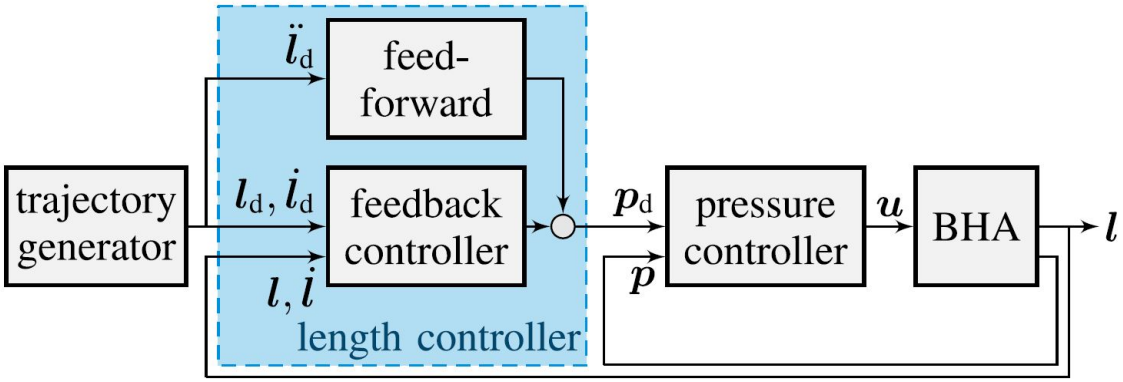

Figure 2.5. Structure of the cascaded control setup with an inner pressure controller and an outer actuator length controller plus an extra actuator trajectory generator [43].

2.3.2. Model-free Controllers

Model-based approaches are not applicable for all soft robots, since the complexities such as hyper-redundancy and nonlinearity result in models that cannot be solved with analytical or iterative methods. Therefore, studies on model-free approaches started which mostly depend on machine learning methods.

Giorelli *et. al.* [44] introduced the first model-free control approach for cable driven soft robots. This approach uses a feed-forward neural network to learn the inverse kinematics. It was experimentally validated for an octopus-like cable driven soft robot that can move in 3D space [33]. A similar method uses a recurrent neural network to learn the kinematics and dynamic models of a soft continuum robot and provides trajectory optimization for predictive control [35]. Another study proposes a position/force controller for soft robots with unknown kinematics, also working in unknown cluttered environment [32]. This controller uses position and force sensors to estimate contact, and machine learning to estimate the Jacobian matrix of a robot. It can control position and force simultaneously.

Machine learning methods are also used to control a class of pneumatic soft robots called "bionic handling assistants". Melingui *et. al.* [38] proposed a model-free approach using supervised learning to control the kinematics, and an adaptive neural network to control the kinetics. Another study used an exploration scheme called online goal babbling [45], which uses bootstrapping to adapt to the kinematics of a bionic elephant trunk while in motion [41].

2.3.3. Hybrid Controllers

Recent studies combine model-based and model-free approaches by using machine learning methods to solve analytical models. For instance, Lakhal *et. al.* [39] proposed an inverse kinematic model, based on parallel rigid robot modeling methods, and used neural networks to approximate the solution of this model. Another study used data-driven modeling for feed-forward control, aiming to increase the accuracy of the controller by using an analytical model together with an error model obtained from machine learning [42].

3. OVERVIEW OF THE ROBOT

Since the control system is designed for a specific robot, mechanical design of the robot should be known to understand the control system. Design of the robot is based on a novel highly-extensible actuator [46]. Actuation principle and mechanical design of the robot are given in detail by Baydere [6].

3.1. Actuation Principle

To understand the actuation principle, it is easier to study it in its simplest form, as a 1-DoF linear actuator. The actuator consists of an inflatable tubing passing through two rollers between which the airway is sealed and the pressure stays only at one side of the rollers as shown in Figure 3.1. The air pressure in the tubing creates a force on the rollers. After passing between the rollers, uninflated part of the tubing, referred as slack, goes back to the base and wrapped around a spool which is controlled by a stepper motor as shown in Figure 3.1b. The air pressure provides the stiffness of body and creates force at the rollers, whereas the motor is used to control speed and position of the actuator, by adding material from the tip.

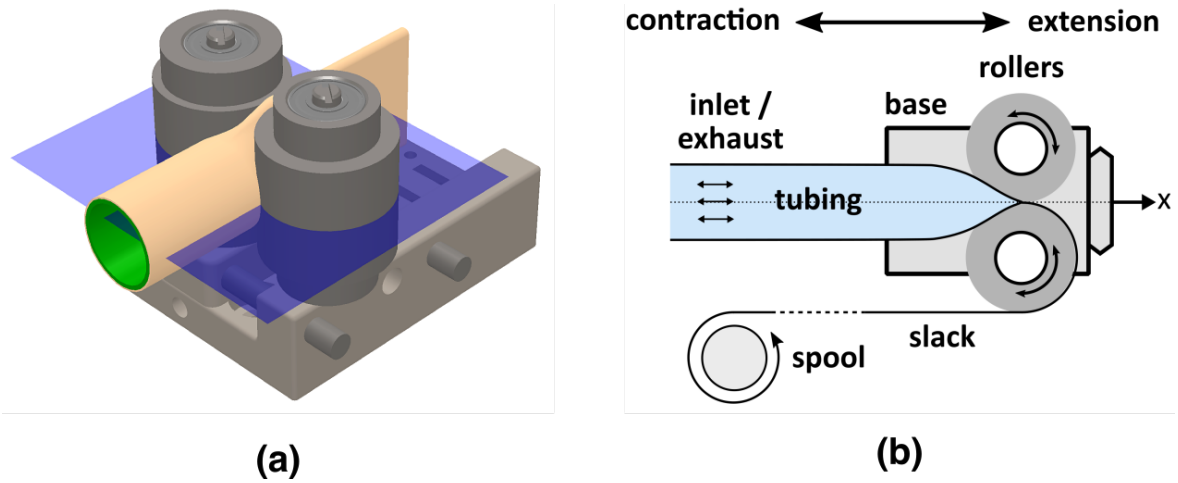

Figure 3.1. (a) CAD drawing of the pinch-roller drive. (b) Section view drawing of the actuator [46].

2-DoF version of the actuator consists of two pinch-rollers placed on the same end-effector in parallel configuration as shown in Figure 3.2. The actuator can move forward and backward, and also rotate on planar surface. Extension and contraction is provided by moving both tubings at the same speed, whereas the rotation occurs by differentiating the speeds of two tubings, e.g. a rotation to the left can be obtained by releasing tubing 2 faster than tubing 1 as shown in Figure 3.2b.

The robot is actuated by three pinch-roller actuators at the end-effector. Rollers are placed at an equal distance to the end-effector center with equal circumferential spacing of 120°. This 3-DoF actuator can move in 3D space with 4 motion primitives which are axial translation, and three pure bendings which occurs by moving only one tubing while keeping the other tubings in same length. Similar to 2-DoF actuator, rotation is provided by mismatched speed of the three tubings, i.e. combining three bendings.

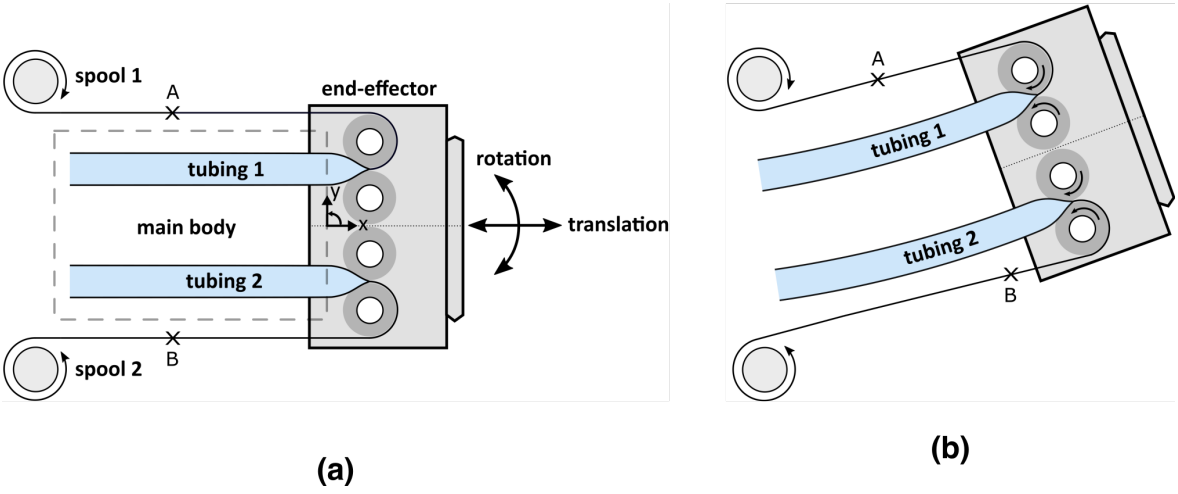

Figure 3.2. (a) Design of the 2-DoF actuator. (b) 2-DoF actuator rotated to the left. See the change in positions of the points A and B from (a) [46].

3.2. Highly-Extensible Soft Continuum Robot

Parts of the robot is analyzed in two main sections which are the robot body and the control hub. The robot body consists of the end-effector at the tip, three inflatable tubings, a backbone, which is a hallow shaft at the center of the tubings that provides extra stiffness, a highly-extensible sheath covering the backbone and inflated part of the tubings. The sheath is used to keep the distance between tubings constant, and to prevent buckling of tubings by creating a single body. The manufactured prototype has 30 cm stroke due to accessibility of appropriate tubings, however, stroke of the robot is only limited by manufacturing capability of the tubings and can be increased using longer tubings. The control hub houses control elements which are explained in detail in Section 4.1. The control hub is separated in two parts which are the air control unit (ACU) and the feed unit (FU) as shown in Figure 3.3. ACU includes the parts to control the air flow, whereas FU includes the parts to control the tubing feed, i.e. length and speed of the tubings.

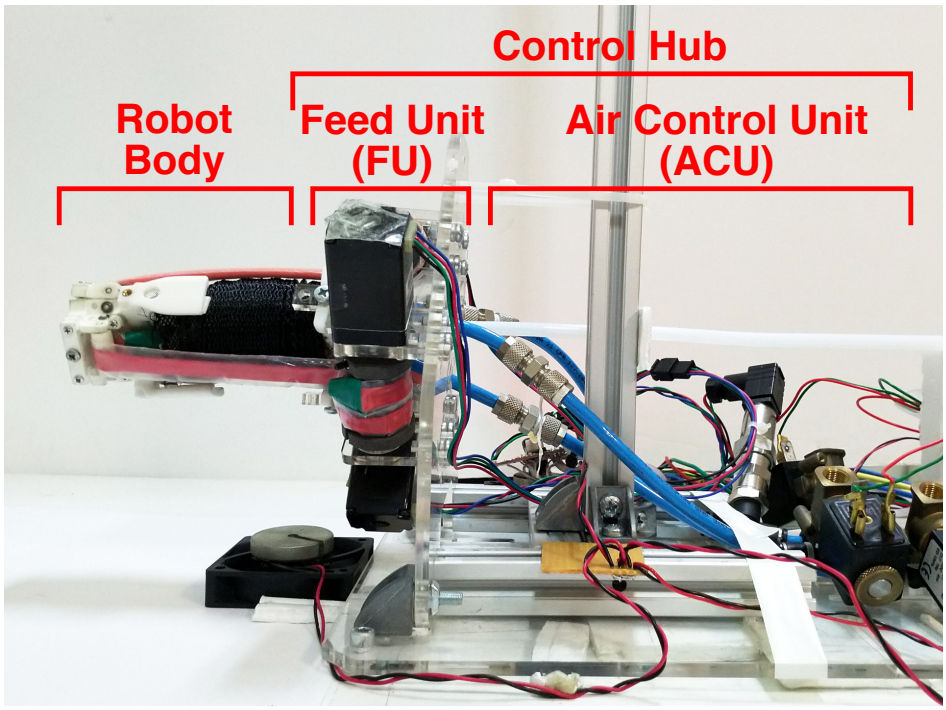

Figure 3.3. Sections of the robot [46].

4. CONTROL SYSTEM DESIGN

The control hub includes an inlet valve, an exhaust valve, a pressure transmitter, and a stepper motor for each tubing. System elements are placed on the control hub as shown in Figure 4.1. Since there are three of each element in the system, the elements associated with the same tubing are numbered from 1 to 3.

An open-loop control system is designed for the robot since there is no sensors to obtain feedback about backbone geometry or end-effector position. The aim of the control system is to obtain an accurate speed and position control. A CompactRIO Real-time Controller (cRIO) of NI Inc. with a built in field-programmable gate arrays (FPGA) and a real-time operating system (RTOS) is used as the processor. The built-in FPGA can work at loop rates up to 40 MHz for analog and digital input/output, whereas the RTOS works at 1 MHz for input/output and mathematical calculations. Inputs and outputs of the cRIO are provided by additional modules. Two modules

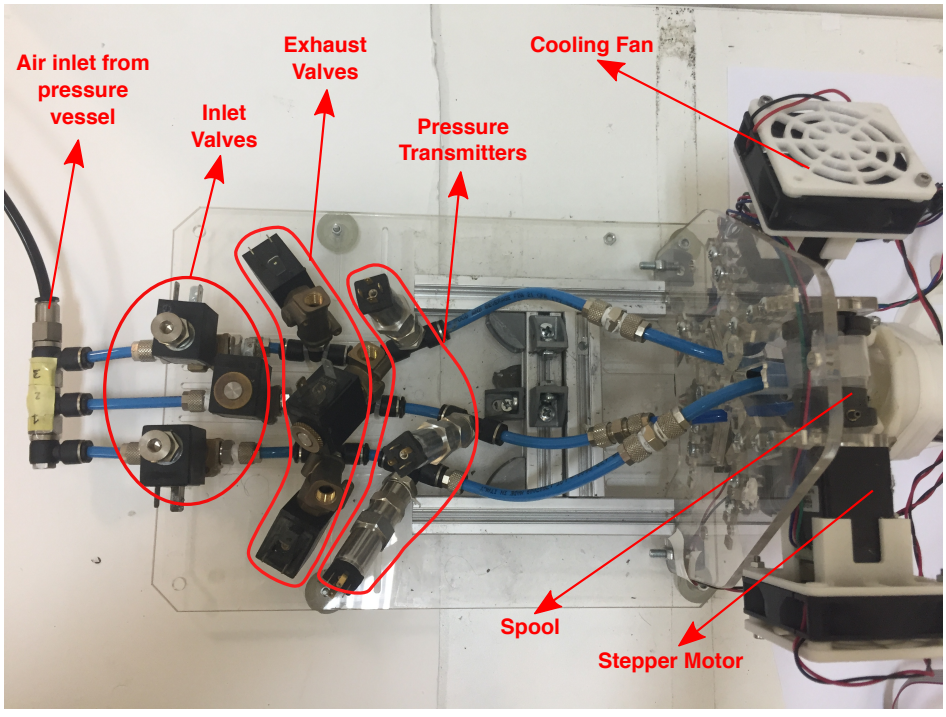

Figure 4.1. System elements in the control hub of the robot.

of cRIO are used in this study which are NI9203 for 4-20 mA analog input (AI), and NI9403 for digital input/output (DIO) (see Appendix A). The control loops are scripted on LabView (NI Inc.) software which is a specific application to easily communicate with cRIO and modules connected to it. Also an interactive GUI is designed on LabView to be displayed on a screen (see Figure B.5), in order to monitor system states and control the system elements from the computer connected to cRIO via network.

Control system schematic of the robot is given in Figure 4.2, which shows the air and electrical signal flow in the system. A dedicated control loop is designed for each individual element to be able to run them at different frequencies. These individual control loops, which are explained in Section 4.1, are run on FPGA for real-time control, whereas all of the computations such as control algorithms and data filtering are done on RTOS.

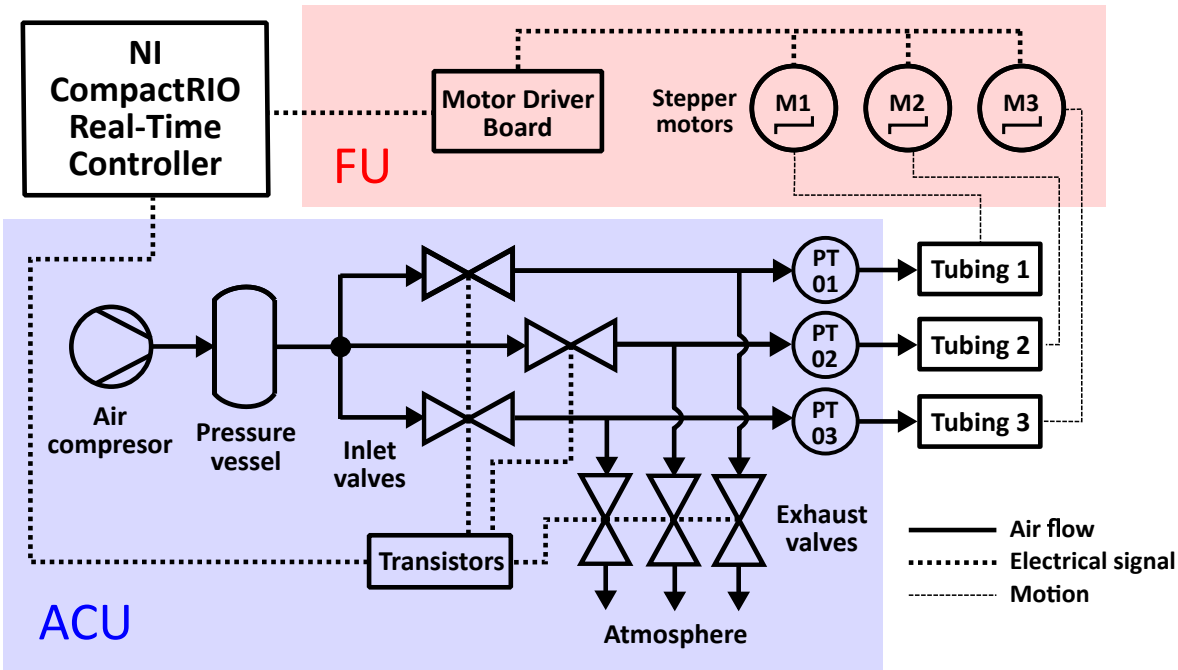

Figure 4.2. Control schematic of the robot [47].

4.1. System Elements

Each system element and its control method are explained individually in this section. Models and specifications of the elements are given in Table 4.1, and the datasheets are given in Appendix A.

Table 4.1. Technical specifications of the control system elements [46].

Component	**Model Name**	**Technical Specifications**
Pressure Transmitter	Keller PA-21Y	0-10 bar, 4-20 mA
Inlet / Exhaust Solenoid Valves	FG Line C01	0-10 bar, 24V, 1 lt/min
Stepper Motor	SY28STH45-0674A	4.5V, 1340 mA, 950 g-cm
Commanding Device	Omega.6	6-DoF data output

4.1.1. Pressure Transmitter

Pressure transmitters with 4-20 mA analog output (AO) are used in the system. The current output of the transmitter is linear with the air pressure. NI9203 AI module is used to read raw analog current data from the transmitters. The module converts the analog input into 16-bit binary data using an ADC as shown in Figure 4.3. This data is then sent to FPGA of cRIO.

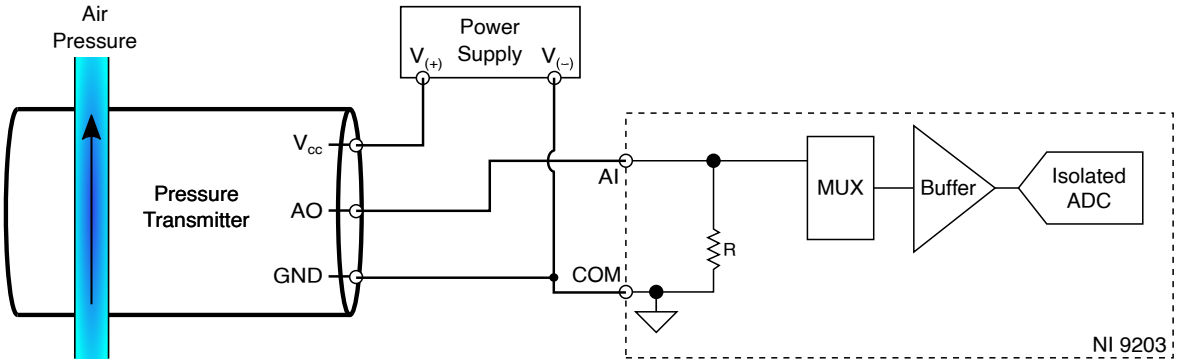

Figure 4.3. Pressure transmitter circuit diagram.

16-bit binary data is converted to decimal in FPGA, which corresponds to current value between 0.004 and 0.020 A, and then sent to RTOS. Data is multiplied with 1000 to convert the input into mA unit for simplicity, and a 100 point moving average filter is applied to the data to reduce noise. Since the pressure transmitter creates AO signal within its full scale, filtered signal (4-20 mA) is interpolated between 0-10 bar, and then converted to kPa by using Equation 4.1, where P is pressure in kPa, and A_{pt} is the filtered input in mA.

$$P = \frac{10}{20-4}(A_{pt} - 4)10^2 \tag{4.1}$$

4.1.2. Solenoid Valves

To control the solenoid valves with fastest response possible, NPN type of bipolar junction transistors are used as switches having a response time of 1 ms. While choosing the transistor and designing the switch circuit shown in Figure 4.4, output current of NI9403 DIO module, I_b, which is 2 mA (see Appendix A), and operating voltage, V_v, and current, I_v, of the solenoid valves are taken as design criteria. Operating current

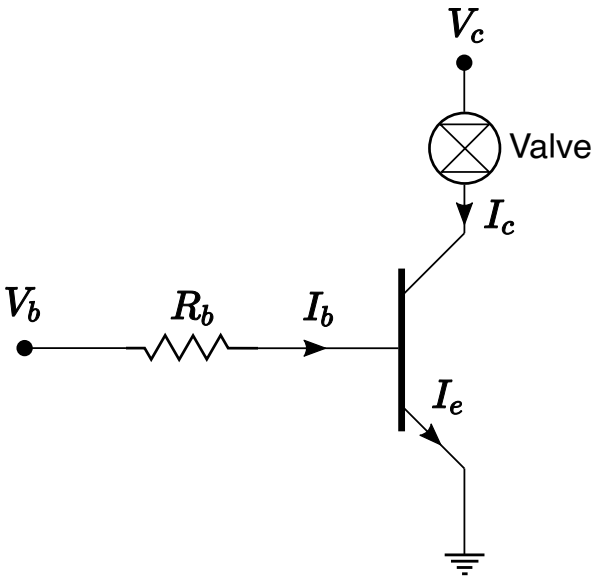

Figure 4.4. Transistor switch circuit.

of the valves are calculated from given power and voltage values in the datasheet as follows: $I_v = W_v/V_v$; where power of the valve, W_v is 5.5 Watts and operating voltage, V_v is 24 V (see Appendix A), thus, the operating current of the valves is $I_v \approx 230$ mA. The output current of NI9403 and operating current of the valves show that a transistor with DC current gain of 115, $\beta_t = I_c/I_b$, is required to be able to provide enough current to open the valve. Adding the operation voltage of the valve as a decision criterion, BD139 NPN transistor with DC current gain of 140, which can operate at maximum collector voltage of $V_c = 80$ V (see Figure A.3), is chosen to use in the switch circuit. Last of all, required base resistance, R_b, is calculated as follows: $R_b = V_b/I_b = 2500\ \Omega$, where V_b is digital signal voltage of 5 V. When the designed circuit gets high digital input (DI), from NI9403 module at base leg, it saturates the transistor and lets the current, $I_c = I_v$, flow through the valve, therefore, opens the solenoid valve since the valves are normally-closed type. When the DI is low, the valve is closed since the transistor is not saturated, therefore, $I_c = 0$. Therefore, the valves can be controlled with simple digital signals with fast response with the designed circuit. It should be noted that the valves have mechanical limitations for the response time.

Flow rate through the exhaust valves has to be controlled during contraction to obtain a steady contraction speed. This is provided through Pulse Width Modulation (PWM) control of the exhaust valves. However, while digital transistor switches work with 1 ms response time, solenoid valves have mechanical limitations that constrain opening/closing times. The solenoid valves have an opening time of 5 ms and closing time of 15 ms. Due to these constraints, duty cycle is limited between 15% and 70% for the chosen PWM period of 40 ms. Outside this range, valves act as either fully closed or fully open.

4.1.3. Stepper Motors

Pololu Nema 11 stepper motors with Sparkfun Quadstepper Motor Driver Board are used in the robot to be able to control the position and speed of the spools. The driver board has a circuit with A4983 micro-step drivers, which can drive the motors in 5 different step resolutions (full, 1/2, 1/4, 1/8, 1/16) using only digital signals. With

the motors having 200 step/round and the driver having up to 1/16 step resolution, motors can be driven with 3200 step/round at maximum resolution, which means a precision of 0.1125 degree/step. Only one driver board is used in the system since the board includes four drivers.

A4983 driver has six DI to control the motors which are ENB (enable power), STEP, DIR (direction), and three MS (microstep) signals to decide the step resolution as given in Figure A.6. Driving the motors at high step resolutions, e.g. 1/16 step, limits the maximum speed that motors can be driven, whereas driving the motors at low step resolutions, e.g. full step, causes vibration at low speeds due to discrete motion. Therefore, step resolution is changed at different speeds that determined empirically as follows:

$$\eta = \begin{cases} 1 \text{ (Full Step, MS1=MS2=MS3=0)} & \omega \geq 200 \\ 1/16 \text{ (Sixteenth Step, MS1=MS2=MS3=1)} & \omega < 200 \end{cases}$$

While MS, ENB, and DIR signals are sent to the driver as simple digital signals, a square wave signal generator is designed for STEP output, considering the working principle of the driver. The driver creates a step pulse for each rising edge of digital

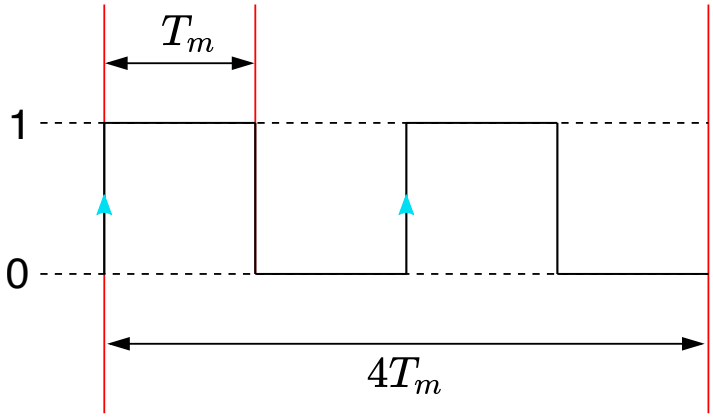

Figure 4.5. Control signal sent to the STEP terminal of the driver. Blue arrows indicate rising edges of the signal.

signal given to the STEP terminal. A function is scripted to send the opposite signal every other loop to the driver. The output signal of the created loop is similar to a PWM signal with 50% duty cycle and period of $2T_m$, where T_m is the loop period of the function. The signal generated during four loops of the function is shown in Figure 4.5, which has two rising edges (indicated with blue arrows), thus, makes the motor move 2 steps. The function also includes a variable called POS to measure motor position. This variable is incremented 16 for full step, and 1 for 1/16 step resolution for each rising edge of the STEP signal. The function is triggered with a boolean variable called MOVE such that square signal is sent to driver if MOVE is positive, otherwise constant STEP signal is sent to driver as shown in Figure 4.6. Sending constant STEP signal to the driver stalls the motors if power is enabled, which is used to brake the spools.

The parameter used to determine motor speed is the period of control loop. As explained above, driver interprets the signal to create one step pulse for motor in every 2 loops. Therefore, the relation between desired motor speed (ω) and control loop period (T_m) is as given in Equation 4.2, where η is step resolution.

$$T_m = \eta \frac{1.5 \times 10^5}{\omega} \tag{4.2}$$

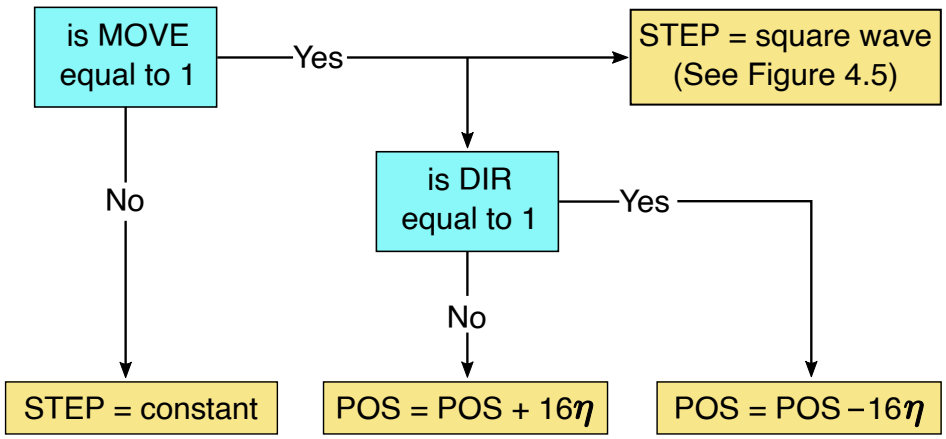

Figure 4.6. Flowchart of the function that measures the motor position and sends the STEP signal to the driver.

4.1.4. Omega.6

The robot is commanded using an omega.6 haptic device (Force Dimension Inc.) for manual navigation. Omega.6 is a 6-DoF delta robot and has a knob for human interaction (see Figure 4.7). The knob position and orientation can be measured by the device, the knob also has a push-button which is used in the control system. Data measured by the device is sent to a computer via USB and then to cRIO via network using the SDK of the device in LabView (see Figure B.4). Following data is processed in RTOS and then used in the teleoperation controller:

- Digital signal of the push-button.
- Position of the knob in longitudinal axis, p_x.
- Orientation of the knob around p_z axis, α.
- Orientation of the knob around p_y axis, β.

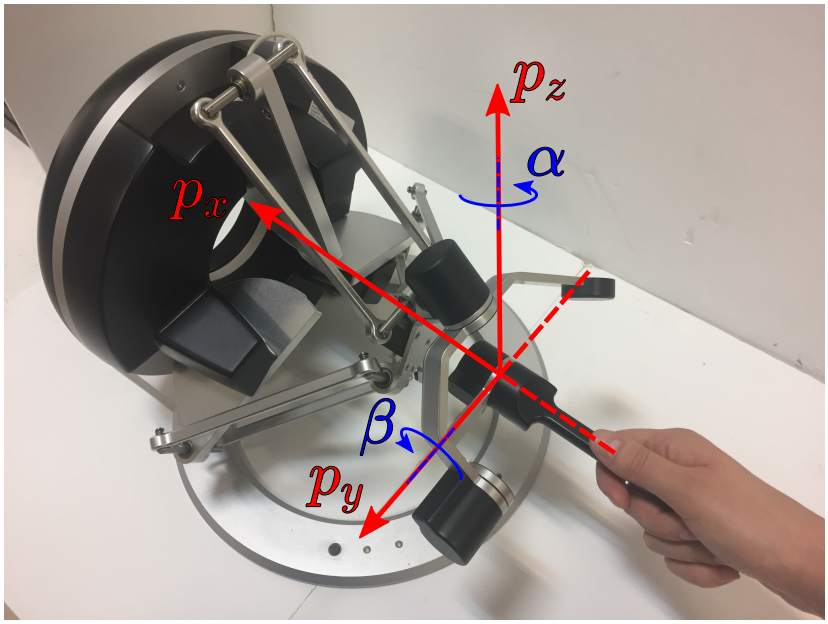

Figure 4.7. Omega.6 haptic device.

4.2. Controllers

Control loops of the system elements given in the previous section are assembled on a single code on the RTOS of the cRIO which is directly connected to the FPGA. This assembled code is the main state controller of the robot. The state controller has a GUI with push-buttons and numerical inputs for control, and also indicators to monitor the tubing pressures and system state (see Figure B.5).

System states are chosen by using three button controls on the GUI which are 'forward', 'backward', and 'stop'. These button controls are programmed as radio buttons such that activating one button disables the other ones. While each button sends its state to the control algorithm, the system state is identified as 'idle' when none of the buttons are active. The idle state is to make mechanical settings of the system such as adjusting roller clearance and rolling the tubings to the spools. In this state, the motors are disabled and free to rotate, the inlet valves are closed, and the exhaust valves are open to keep the tubings unpressurized.

In the forward state, both motors are enabled, MOVE input is positive, direction of the motors are set to release the tubings from the spools, the inlet valves are open to pressurize the tubings, and the exhaust valves are closed. Differences between the backward and forward states are direction of the motors, and the exhaust valve control. The exhaust valves are controlled with PWM input in the backward state to release the extra pressure caused by the decrease in the volume.

In the stop state, the inlet valves are open, the exhaust valves are closed, and the motors are enabled, however MOVE input is negative to brake the spools using holding torque of the motors. Also, the motors are given full step input in stall position to increase the holding torque with full phase control. In this state motors are overheated due to constant current to create the holding torque, therefore, cooling fans are added to the system to cool down the motors. The control algorithm depending on the state input is given in Figure 4.8.

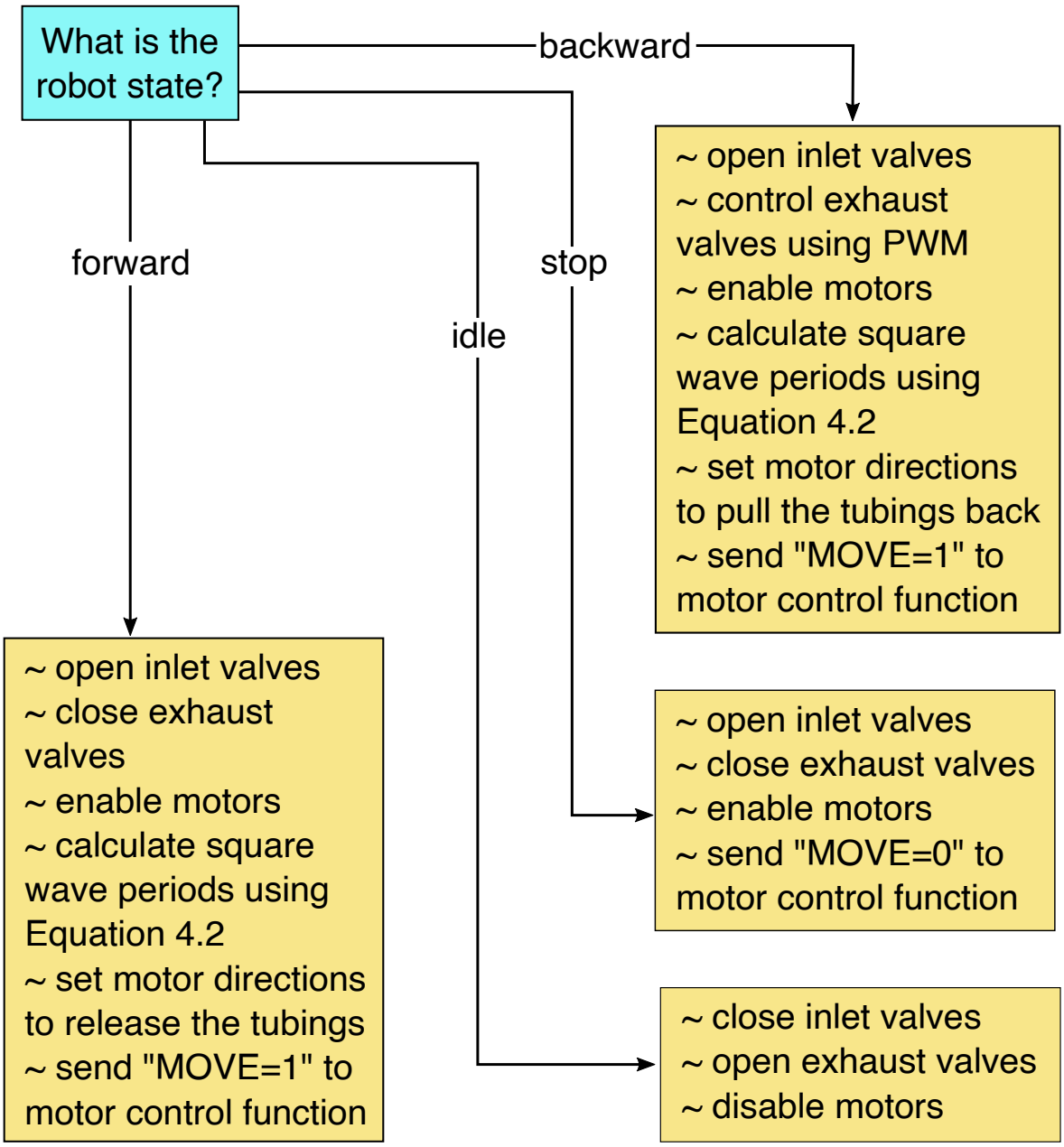

Figure 4.8. Main state controller algorithm.

4.2.1. Speed Controller

An open-loop speed controller is designed for straight extension and contraction of the robot. To control the end-effector speed, required motor speeds should be calculated, and the motors should be rotated at the same speed synchronously to prevent any rotation. Considering Figures 3.1 and 3.2, each tubing can be modeled

as a simple parallel pulley system, therefore, end-effector speed should be equal to the half of the tangential speed of the spools. Then the relation between angular speed of motors and the translational speed of the end-effector should be as given in Equation 4.3 where ω is the motor speed in rpm, v_{ee} is end-effector speed in mm/s, and r_{sp} is spool radius in mm. After obtaining the required motor speed, ω, it is sent to the control loop of the motors given in Section 4.1.3 to calculate the period of the control loop using Equation 4.2. Consequently, user input for end-effector speed is sent to the motors as follows: $v_{ee} \rightarrow \omega \rightarrow T_m$.

$$\omega = \frac{2v_{ee}}{r_{sp}} \frac{60}{2\pi} \tag{4.3}$$

4.2.2. Position Controller

A rudimentary kinematic model is developed to calculate the inverse kinematics of the robot for the position controller [48]. Constant curvature approach is used to model the length of the backbone and the tubings using a method similar to the one described by Webster et al. [27].

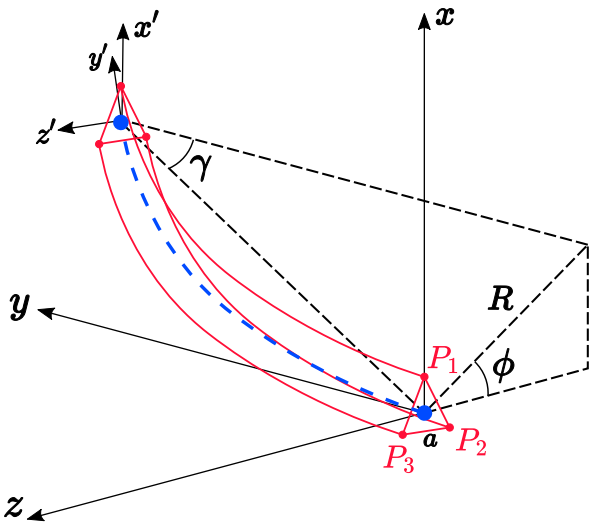

Figure 4.9. Modeling of the tubings and backbone of the robot. Tubings are shown as red solid lines and the backbone is shown as blue dashed line [47].

We assumed the slope of the body at start point is zero, i.e. tubings and backbone are perpendicular to xz-plane, and the distance between the tubings, $|P_1P_3| = |P_3P_2| = |P_2P_1| = a$, is constant through the body as shown in Figure 4.9. Tip position is taken as the middle of the end effector, which is also the tip of the backbone. The backbone length, S_b, and tubing lengths S_1, S_2, S_3 are calculated from the tip position given in global coordinates x, y, z, by using Equations 4.4 to 4.7. The configuration space parameters used in these equations are the rotation angle with respect to the fixed frame y axis, ϕ, the angle between z'-axis and the straight line between origin and goal point, γ, and radius of curvature of the backbone, R.

$$S_b = R(\pi - 2\gamma) \tag{4.4}$$

$$S_1 = \left(R - sin\phi\left(\frac{a\sqrt{3}}{3}\right)\right)(\pi - 2\gamma) \tag{4.5}$$

$$S_2 = \left(R - sin(\phi - 2\pi/3)\left(\frac{a\sqrt{3}}{3}\right)\right)(\pi - 2\gamma) \tag{4.6}$$

$$S_3 = \left(R - sin(\phi - 4\pi/3)\left(\frac{a\sqrt{3}}{3}\right)\right)(\pi - 2\gamma) \tag{4.7}$$

where,

$$\phi = \begin{cases} tan^{-1}\left(\frac{x}{z}\right) & z \geq 0 \\ \pi + tan^{-1}\left(\frac{x}{z}\right) & z < 0 \end{cases} \tag{4.8}$$

$$\gamma = tan^{-1}\left(\frac{ysin\phi}{x}\right) \tag{4.9}$$

$$R = \frac{y}{sin(\pi - 2\gamma)} \tag{4.10}$$

After the tubing lengths are calculated for input coordinates, they are converted to motor position. By integrating Equation 4.3, relation between motor position and tubing lengths are obtained and given in Equation 4.11. In order to release all tubings in the same time interval, motors are rotated in different speeds depending on the calculated tubing length. The fastest tubing speed is decided by user input v_{test}, and then converted to motor speed using Equation 4.3 to calculate individual motor speeds for the test using Equation 4.12.

$$\theta_i = \frac{2S_i}{r_{sp}} \tag{4.11}$$

$$\omega_i = \omega_{test} \frac{\theta_i}{max(\theta_1, \theta_2, \theta_3)} \tag{4.12}$$

Since the motor position is measured in steps unit, calculated motor position is converted to step unit from radian, to use it in the control algorithm. Step resolution, η is set to 1/16 since the position tests does not require high speeds. Therefore, the motor position unit is converted to steps using Equation 4.13, where Θ is motor position in steps and θ is motor position in rad.

$$\Theta_i = \theta_i \frac{3200}{2\pi} \tag{4.13}$$

After calculating the control parameters, user starts the position control to move the robot from zero position to input position (x, y, z). The position control algorithm sends system state and motor speed data to main control algorithm to move the robot while reading position data from motor control loops as shown in Figure 4.10.

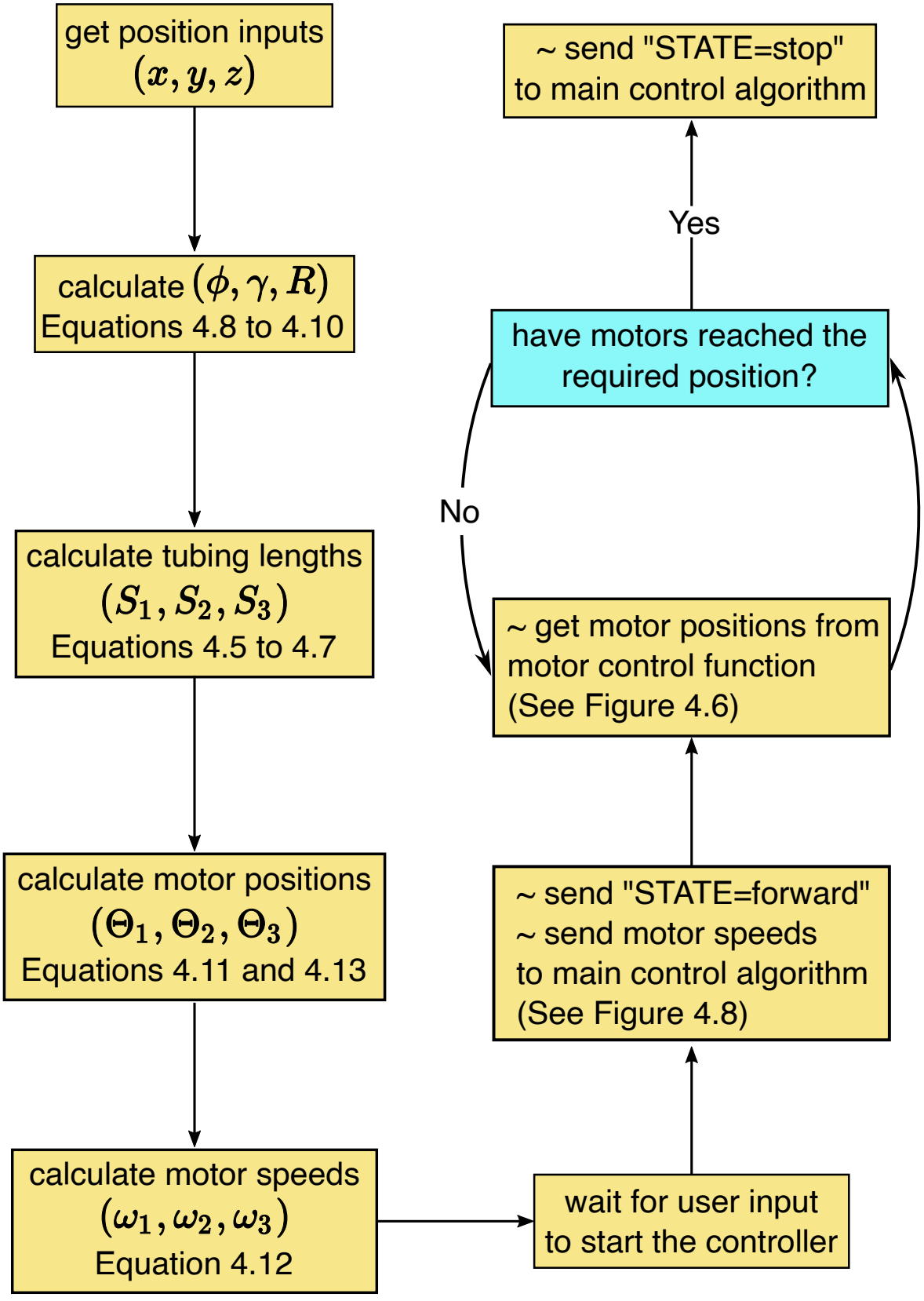

Figure 4.10. Algorithm of the position controller.

4.2.3. Teleoperation Controller

A teleoperation controller is designed and the omega.6 is used as the commanding device. Position output, p_x, and orientation outputs, α and β, and push-button output data of the omega.6 are used to command the robot. p_x data of omega.6 is mapped into real world coordinates which is ± 60 mm from the workspace center of the device. α and β outputs of the omega.6 is $\pm 100^\circ$ from the straight state of the knob which does not require any mapping. Push-button output is a digital signal and used as a boolean data.

Sign of the p_x output is used to decide direction state of the robot, forward or backward, i.e. extension or contraction, respectively. A dead-zone is identified such that $|p_x| < 10$ mm to identify the stop state. End-effector speed is calculated by mapping $|p_x|$ data from 10 to 60 mm between predefined user inputs v_{min} to v_{max} as shown in Equation 4.14. This end-effector speed is then converted to motor speed ω, using Equation 4.3.

$$v_{ee} = \frac{v_{max} - v_{min}}{60 - 10}(|p_x| - 10) + v_{min} \tag{4.14}$$

Steering direction of the robot is decided from the wrist orientation i.e. from inputs α and β. These two input angles are used as a 2D coordinate system to determine direction and curvature of the steering. $\lambda = atan2(\beta, \alpha)$ is used to determine the steering direction, whereas $r_\lambda = \sqrt{\alpha^2 + \beta^2}$ is used to determine the curvature of the steering.

There are six predefined steering directions of the robot, three of them are towards each tubing, and other three in the opposite direction of the first three. The coordinate system created using α and β forms a circle of diameter 100°, and this circle is divided into six regions which are called region 1, 2, 3, 1-2, 1-3, and 3-2 as shown in Figure 4.11. The robot is rotated toward the center of the region that contains the point $P_\lambda(\alpha, \beta)$.

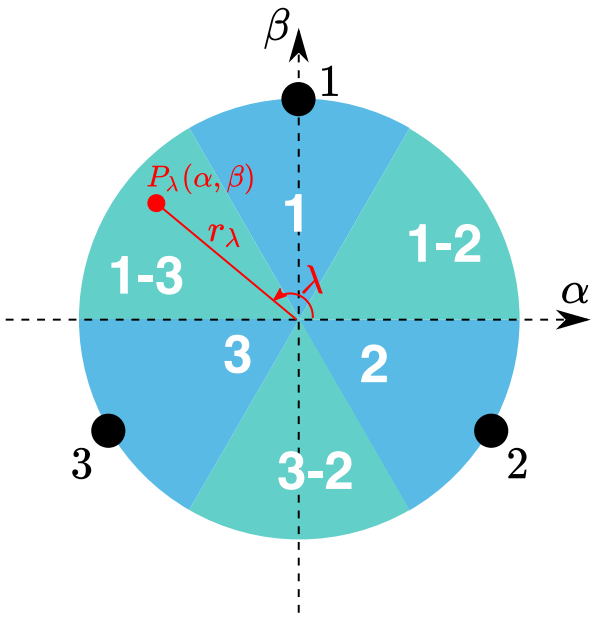

Figure 4.11. Illustration of steering inputs α and β and rotation regions in teleoperation controller. Tubing positions are shown with black circles.

Similar with the elongation/contraction control, a dead-zone is designed for steering such that there is no rotation for the cases $r_\lambda < 45$. For the wrist orientation $r_\lambda \geq 45$, i.e. when there is a rotation, the faster motor or motors rotates with calculated ω value, whereas the slower motor or motors rotates with speed ω_{slow} which varies between $\omega/2$ and ω. ω_{slow} is calculated as a function of r_λ as shown in Equation 4.15. The difference between ω and ω_{slow} decides the curvature of the steering.

$$\omega_{slow} = \omega - \frac{\omega/2}{100-45}(r_\lambda - 45) \tag{4.15}$$

The algorithm deciding the system state and calculating motor speeds depending on the user inputs is given in Figure 4.12. The outputs of the algorithm (STATE, ω_1, ω_2, ω_3) are then sent to the main control algorithm given in Figure 4.8.

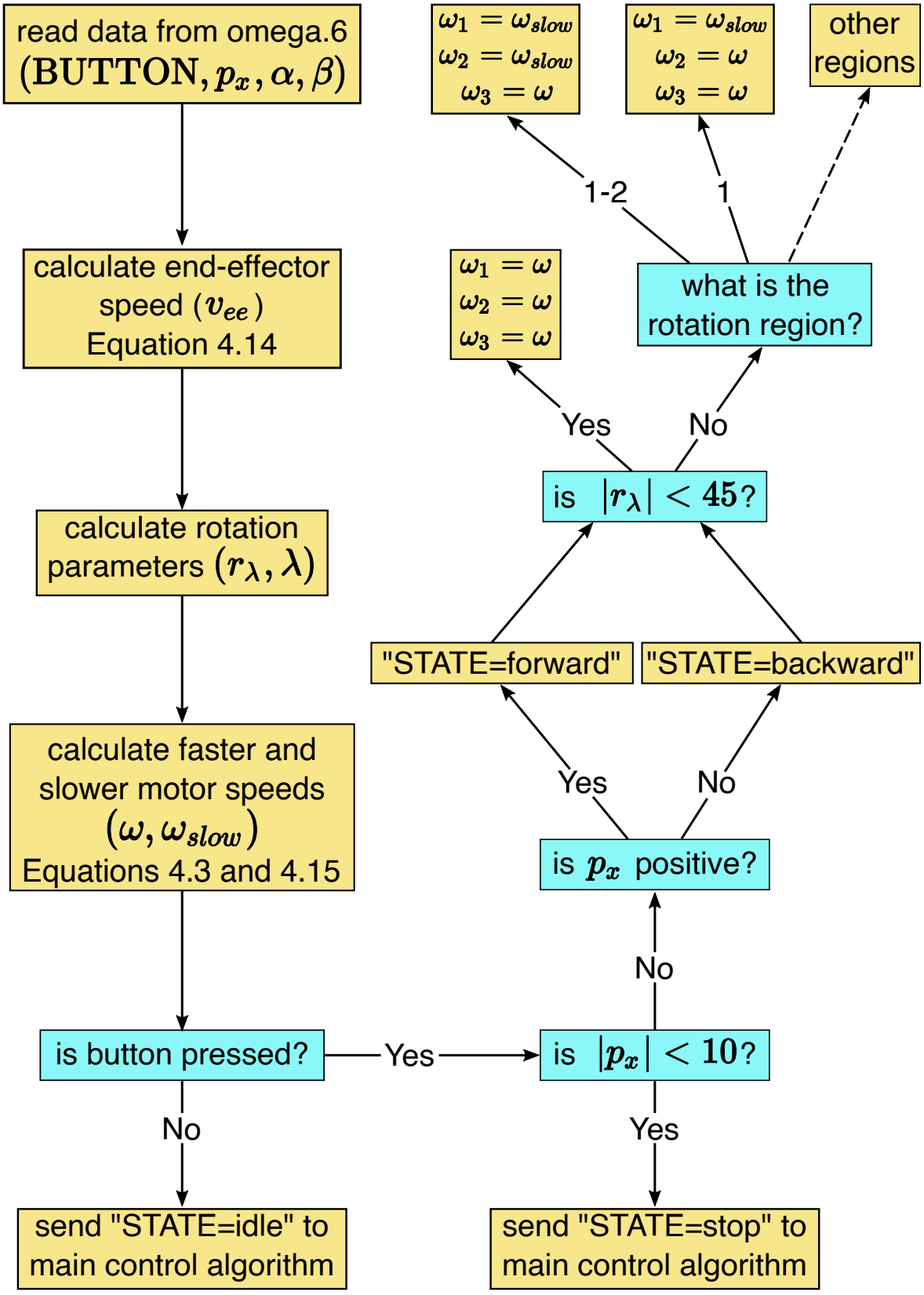

Figure 4.12. Algorithm of the teleoperation controller.

5. EXPERIMENTAL METHODS

Experiments were performed to test the speed, position and teleoperation controllers. In this chapter, methods followed during the experiments are explained.

5.1. Speed Tests

To test the designed speed controller, end-effector speed for straight extension was measured by mounting two push buttons, one at the start and one at the end position of the test setup. Push-button data were read via FPGA with a sampling rate of 1 ms. The buttons were placed at a distance of 62 mm which is equal to the total distance traveled by the end-effector during tests. The speed controller was tested at input speeds of 20, 50, 100, 150, 200, 250 and 300 mm/s at a fixed 100 kPa tubing pressure. Speeds higher than 300 mm/s were not attainable due to the mechanical limitations.

Each test was performed by resetting the end-effector position (i.e. moving it until it reaches the start button) and then moving the robot at a constant speed. Average speed was calculated by recording the time elapsed from leaving the start button to reaching the end button. Five trials were performed at each motor speed input, and the mean value was taken into consideration.

5.2. Position Tests

The open-loop position controller was tested at different input coordinates by measuring the actual tip position and calculating the mean error at each point. The coordinates were chosen such that 5 points were tested at each xz-plane at longitudinal distances of $y = 100, 125, 150, 200$ mm. Thus, 20 points were tested in total. 5 trials were performed at each point. A total of 100 trials were conducted at constant tubing pressure of 140 kPa. After each test, robot position was reseted to start position programmatically from the measured motor positions.

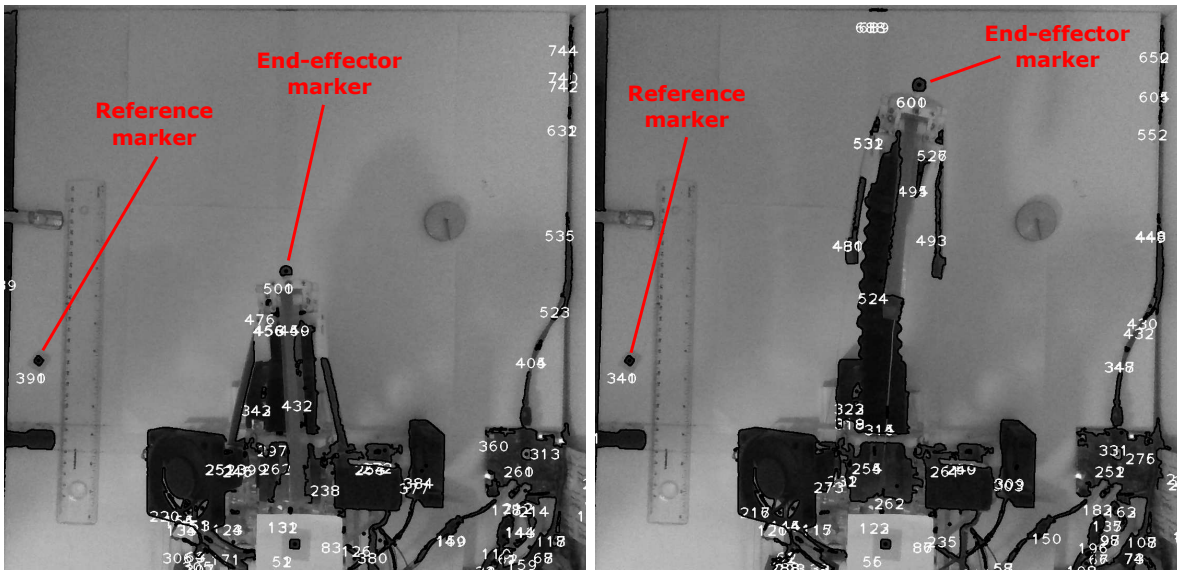

Figure 5.1. Processed image at the start position (left) and at the end position (right).

An Intel RealSense D435 depth camera (having integrated stereo camera, RGB module and infrared projector, with RMS depth error $\leq$ 2%) was used to track a colored circle-shaped marker at the robot tip at the initial and final locations. To evaluate the marker position, the RGB and depth images taken with the camera were aligned and then the RGB image was segmented to find the center pixel of the marker to extract the 3D position data from depth image. Another marker was also used with known position as a reference point in order to calculate the marker position relative to that point as shown in Figure 5.1. After identifying the marker labels, the 3D data was converted into millimeters to compare the measured position with the input position.

5.3. Teleoperation Tests

Teleoperation controller was tested in terms of user experience and navigation abilities of the robot. To test the controller, three users commanded the robot via the omega.6 to extend, contract and rotate the robot in order to reach a target in free space. The controller was also tested in an enclosed path and an obstacle course where users tried to reach the target by avoiding any collision. The controller was evaluated by observation and user feedback, and no quantitative tests were conducted.

6. RESULTS AND DISCUSSION

Results of each controller experiment are given in this chapter. Considering the obtained results, performance of the controllers are also discussed.

6.1. Speed Controller Results

The absolute and relative errors between the input and the measured robot tip speed are given for input speeds between 20-300 mm/s as box plots in Figure 6.1. Red points represent the mean for each data set whereas solid line represents the median. The minimum and maximum relative errors were 1.1% and 4.4% at 100 and 300 mm/s, respectively. The input speed vs. measured speed with standard deviation, 3σ, is given in Figure 6.2.

The root-mean-square error (RMSE) of the overall speed tests was calculated as 2.7%. Some problems that may cause error in measured speed could be the pauses during motion due to jamming of the rollers and non-uniform coiling of the tubings on the spools. Mechanical revisions for the end-effector and spools may provide a more accurate speed control. Other than mechanical problems, experimental method could

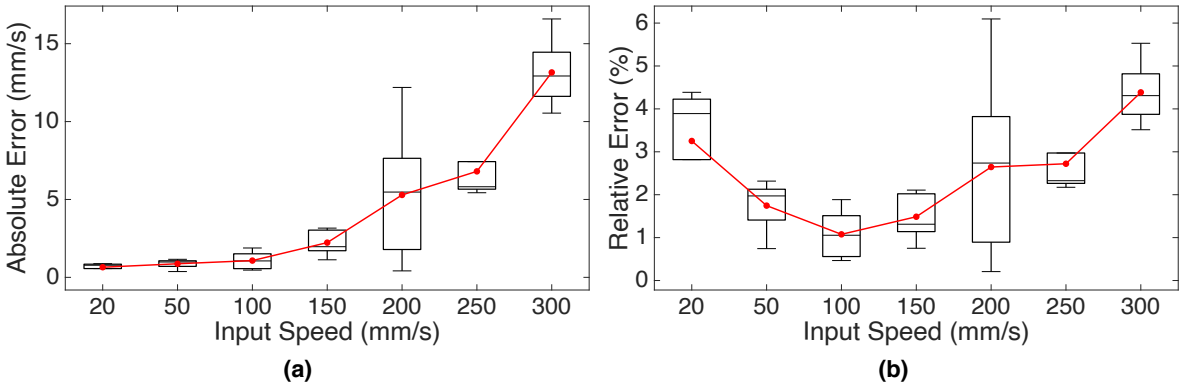

Figure 6.1. (a) Absolute and (b) relative error in speed controller [47]. Red points represent the mean data whereas the solid line represents the median of 5 trials.

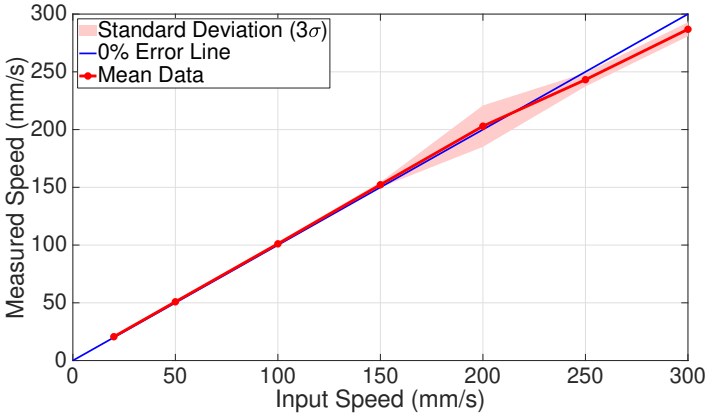

Figure 6.2. Input and measured speed of the end-effector. Red circles represents the mean measured speed data, whereas the shaded area represents the standard deviation of 5 trials. 0% error line is also given for a better comparison.

be improved to obtain more accurate results since the acceleration of the robot was not taken into account during speed measurements which also increased the error at higher speeds. Using a high speed camera and measuring the speed after the end-effector reaches the terminal speed may increase the accuracy of the measurements.

6.2. Position Controller Results

Position test results are given in Figure 6.3 as 2D projection graphs at axial elongation inputs (y) of 125 and 200 mm, and also as a 3D graph of all the test points for comprehensive understanding. The solid points represent the given goal position. Shaded volumes represent standard deviation of each measured data set. The input and mean measured positions are marked and distance to the measured position is drawn as a dashed line in 2D projection graphs. The color of the points represents the mean error where error is the distance between input and measured tip position in millimeters. The calculated mean error was 13.8, 13.4, 14.4, and 22.6 mm for a longitudinal distance (y) of 100, 125, 150, and 200 mm, respectively. All errors were less than half of the robot's outer diameter (55 mm). Minimum error was 5.5 mm with the robot in straight extension at the goal position $(0, 125, 0)$, whereas maximum mean error was 30 mm at $(0, 200, 50)$.

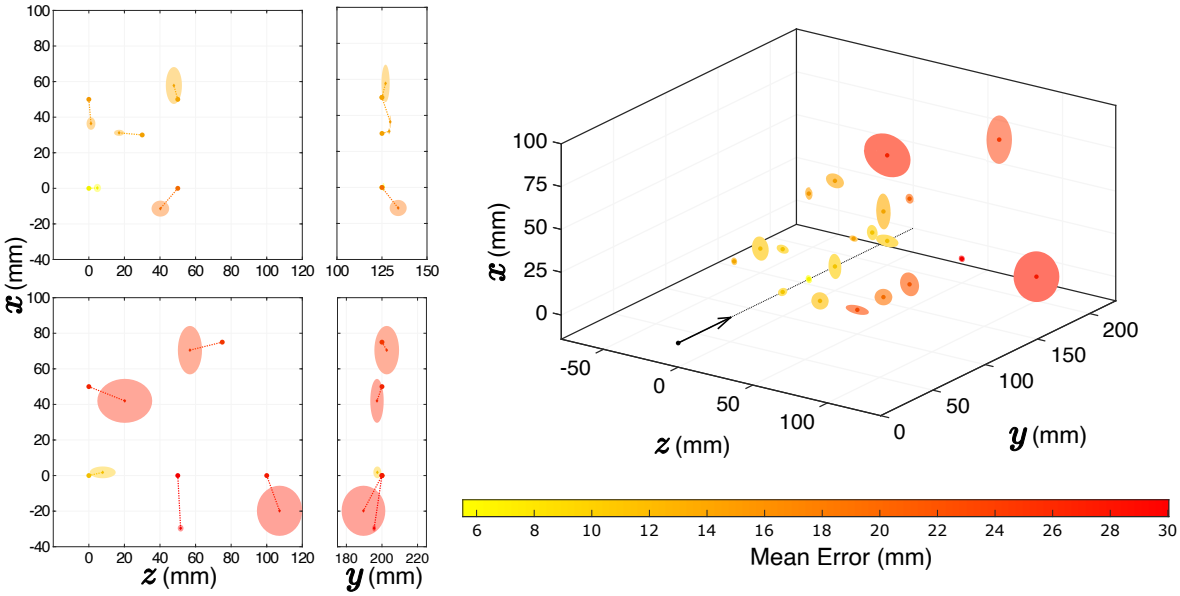

Figure 6.3. Input position vs. measured position for axial elongation of 125 mm (left-top), and 200 mm (left-bottom), projected on 2D graphs. The mean error of 5 trials for all tested points in the workspace shown on 3D graph (right) [47].

Majority of the calculated mean error came from deflection of the tip in x-direction due to weight of the end effector. The x-component of mean error was -5.32, -8.41 and -15.5 mm for longitudinal distances (y-direction) of 100, 150, and 200 mm, respectively. As expected, this error was more prominent at points farther from the robot base, reaching around 4 times the second largest error component at a y-distance of 200 mm. The second largest error component was 2.9, 3.7 and -3.7 mm for 100, 150 and 200 mm y-distance respectively, all in the y-direction.

To support the claim of the effect of gravity on errors in position test results, the bending stiffness data of the robot given by Baydere [6] were used to calculate the expected tip deflection due to gravity. The deflection values were calculated as -3.2, -7.1 and -12.3 mm at longitudinal distances, 100, 150, and 200 mm, respectively. Although the calculated deflections are lower, they are still consistent with the mean errors in x-direction. The bending stiffness data can be used to estimate and compensate the effect of gravity in the position controller by adding a correction factor into the model from known variables, i.e. the body length and corresponding bending stiffness.

6.3. Teleoperation Results

Cognitive workload of usability of the teleoperation controller was evaluated as low by the users, since the speed of the robot was controlled by moving the knob forward, pointing the knob into a direction provided the rotation. Robot was successfully commanded to reach a target in free space, through obstacles and in an enclosed path by all users. The time lapse images of the experiments are given in Figures 6.4, 6.5, and 6.6.

The maximum curvature of rotation was not enough for the tight bend shown in Figure 6.6, since the curvature of rotation was predefined. Therefore, a user input was added to GUI to scale ω_{slow}, in order to alter the steering ability of the robot. The reason of adding an interactive user input instead of permanently changing the steering ability was that the robot body buckles at high curvature rotations without any external support. Therefore, the interactive input provides the ability to change the steering curvature while navigating the robot through an environmental transition, e.g. from a cluttered environment to free space.

A repeatable contraction was not achieved, because buckling occurred at robot body at high stiffness, i.e. exhaust valves at low PWM duty cycle. And the end-effector weight caused collapse at low stiffness, i.e. exhaust valves at high PWM duty cycle.

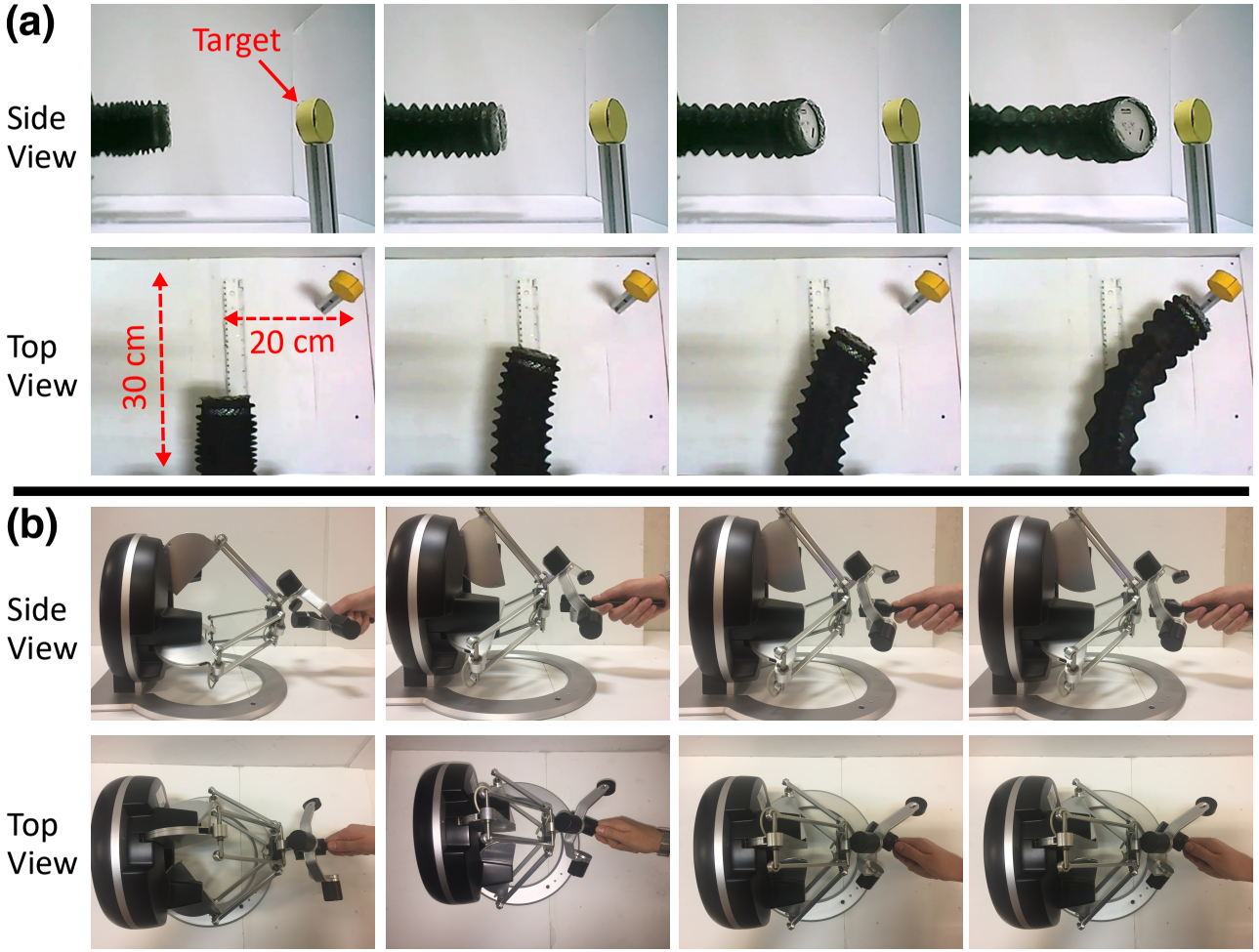

Figure 6.4. Time lapse of teleoperation test in free space. (a) The shape of the robot body, (b) position and orientation of the omega.6 knob.

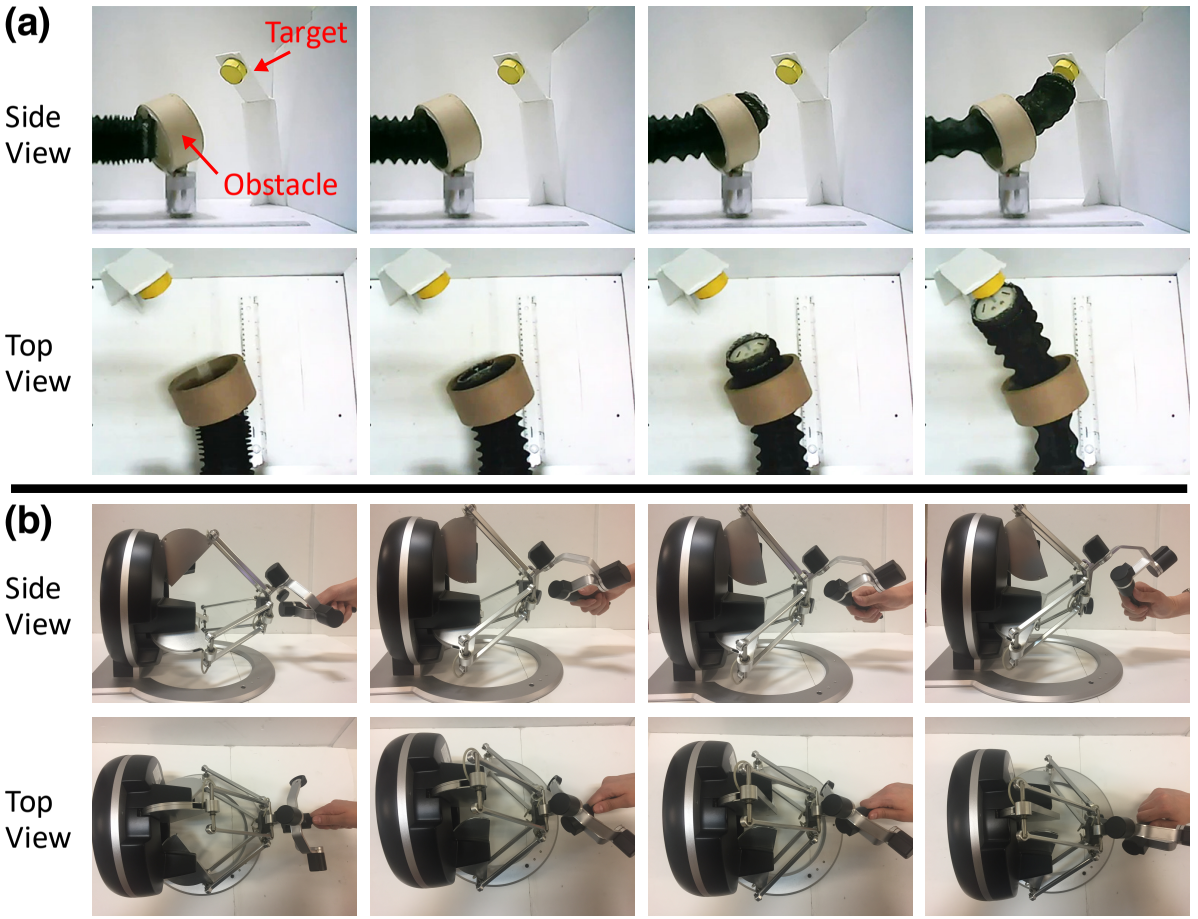

Figure 6.5. Time lapse of teleoperation test through an obstacle. (a) The shape of the robot body, (b) position and orientation of the omega.6 knob.

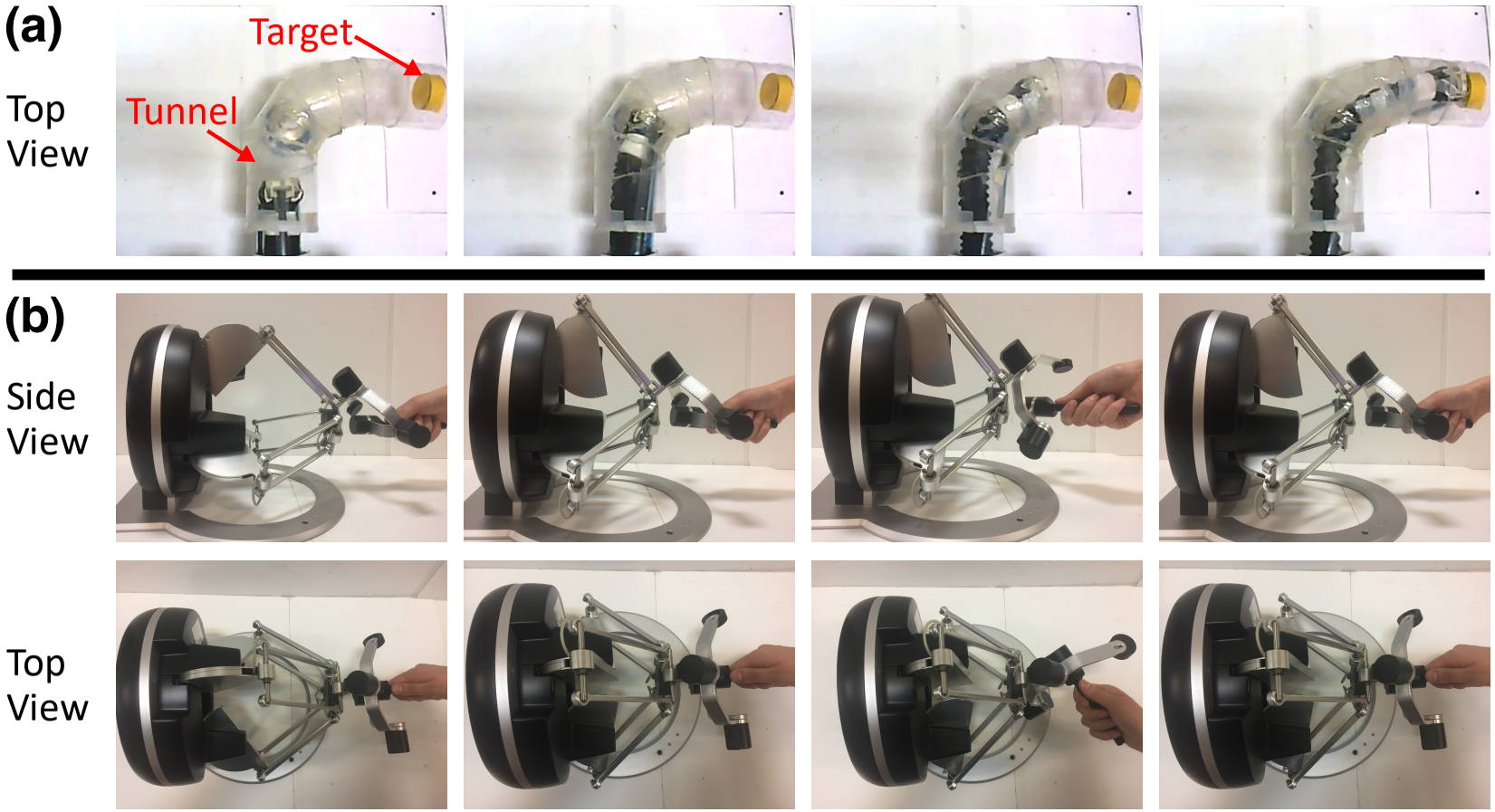

Figure 6.6. Time lapse of teleoperation test in an enclosed path. (a) The shape of the robot body, (b) position and orientation of the omega.6 knob.

7. CONCLUSION

In this study, control system of a novel extensible soft continuum robot has been designed, developed and tested. Control system includes the individual control systems of mechatronics components (circuits, drivers, control codes), and the open-loop speed, position and teleoperation controllers of the robot. The open-loop speed controller achieved an accurate extension with overall root-mean-square error of 2.7%. As a consequence of mechanical issues such as jamming of rollers, relative error increased at higher speeds. The speed controller could not be tested for contraction because of the buckling of the robot body. The open-loop position controller performed with a maximum mean error of 22.6 mm at longitudinal input of 200 mm, which is lower than the radius of the robot body. Since the stiffness decreases as the robot extends, error in the position controller increased as the body length increased, mostly in the gravitational direction. The teleoperation controller is found to be intuitive to map the position and orientation of human wrist into speed and steering direction of the robot. The robot is navigated from a zero position to a target position in various scenarios using an omega.6 as the commanding device. A repeatable contraction was not achieved for teleoperation tests because of the buckling of robot body.

7.1. Contributions and Originality

The originality of this study is provided by novelty of the actuator. The main difference and the most prominent advantage of the robot compared to other pneumatic soft robots in the literature is decoupling of the chamber pressure and the tip speed. This advantage provides simpler modeling and more accurate speed and position control. Another novelty of the robot is that it extends by adding material from the tip, i.e. by growing like a plant, instead of elastic deformation. Since the movement is not provided by material deformation, there is no energy loss due to high strains. There are several other growing robots in the literature [49, 50], however, they do not have active steering ability.

This study contributed to the literature as a journal article presenting a novel 2-DoF actuator [46], and a conference paper presenting a colonoscope design based on the actuator [51]. There are also two journal articles in review which present the design and development of the highly-extensible soft robot [47], and the quasi-static model developed for the robot [48].

7.2. Outlook and Future Work

The proposed highly-extensible soft continuum robot and the validated controllers are promising for many applications such as inspection, urban search and rescue, and minimally invasive surgery. The robot design allows a channel through the hallow backbone which can be used to insert a camera or manipulation tools. Open-loop teleoperation controller together with camera guidance from the tip is expected to allow the robot to be navigated through clustered environments easily.

Considering the experimental results, some revisions for the model and controllers should be considered as future work. Weight of the body and the end-effector may cause some problems in free space applications. Therefore, the error caused by the weight of the end-effector should be reduced by adding a weight compensation to the position model. Another problem during the tests was the buckling of the robot body during contraction. To overcome this problem, a pressure controller with high precision should be designed. Also, it was seen that the system has a high response time and no real-time controller was required to control the robot, therefore, a cheaper and simpler micro-controller can be used for the robot.

For future applications, some additional features may be added especially to increase the body stiffness. Considering a general manipulation case, a steady robot tip is required. This can be provided by increasing the stiffness by using methods similar to the ones given by Langer *et. al.* [52]. Other than increasing the stiffness, a magnetic or vacuum anchor can be added to the robot tip to stabilize the end-effector. Also, for medical applications such as endoscopy or minimally invasive surgery, the robot can be downscaled, or for search and rescue operations, robot can be upscaled.

REFERENCES

1. Taylor, R., "A Perspective on Medical Robotics", *Proceedings of the IEEE*, Vol. 94, No. 9, pp. 1652–1664, sep 2006.

2. Cianchetti, M., M. Calisti, L. Margheri, M. Kuba and C. Laschi, "Bioinspired locomotion and grasping in water: the soft eight-arm OCTOPUS robot", *Bioinspiration & Biomimetics*, Vol. 10, No. 3, p. 035003, may 2015.

3. George Thuruthel, T., Y. Ansari, E. Falotico and C. Laschi, "Control Strategies for Soft Robotic Manipulators: A Survey", *Soft Robotics*, Vol. 5, No. 2, pp. 149–163, apr 2018.

4. Trivedi, D., A. Lotfi and C. Rahn, "Geometrically Exact Models for Soft Robotic Manipulators", *IEEE Transactions on Robotics*, Vol. 24, No. 4, pp. 773–780, aug 2008.

5. Ganji, Y. and F. Janabi-Sharifi, "Catheter Kinematics for Intracardiac Navigation", *IEEE Transactions on Biomedical Engineering*, Vol. 56, No. 3, pp. 621–632, mar 2009.

6. Baydere, B. A., *Design of a Highly-extensible Pneumatic Actuator for Soft Robotic Applications*, M.Sc. Thesis, Bogazici University, 2019.

7. Laschi, C., B. Mazzolai and M. Cianchetti, "Soft robotics: Technologies and systems pushing the boundaries of robot abilities", *Science Robotics*, Vol. 1, No. 1, p. eaah3690, dec 2016.

8. Cianchetti, M., T. Ranzani, G. Gerboni, T. Nanayakkara, K. Althoefer, P. Dasgupta and A. Menciassi, "Soft Robotics Technologies to Address Shortcomings in Today's Minimally Invasive Surgery: The STIFF-FLOP Approach", *Soft Robotics*, Vol. 1, No. 2, pp. 122–131, jun 2014.

9. Laschi, C., M. Cianchetti, B. Mazzolai, L. Margheri, M. Follador and P. Dario, "Soft Robot Arm Inspired by the Octopus", *Advanced Robotics*, Vol. 26, No. 7, pp. 709–727, jan 2012.

10. Walker, I. D., D. M. Dawson, T. Flash, F. W. Grasso, R. T. Hanlon, B. Hochner, W. M. Kier, C. C. Pagano, C. D. Rahn and Q. M. Zhang, "Continuum robot arms inspired by cephalopods", G. R. Gerhart, C. M. Shoemaker and D. W. Gage (Editors), *SPIE*, Vol. 5804, p. 303, International Society for Optics and Photonics, may 2005.

11. Onal, C. D. and D. Rus, "Autonomous undulatory serpentine locomotion utilizing body dynamics of a fluidic soft robot", *Bioinspiration & Biomimetics*, Vol. 8, No. 2, p. 026003, mar 2013.

12. Shepherd, R. F., F. Ilievski, W. Choi, S. A. Morin, A. A. Stokes, A. D. Mazzeo, X. Chen, M. Wang and G. M. Whitesides, "Multigait soft robot.", *Proceedings of the National Academy of Sciences of the United States of America*, Vol. 108, No. 51, pp. 20400–3, dec 2011.

13. Walker, I. D., "Biologically inspired vine-like and tendril-like robots", *2015 Science and Information Conference (SAI)*, pp. 714–720, IEEE, jul 2015.

14. Dong, X., D. Axinte, D. Palmer, S. Cobos, M. Raffles, A. Rabani and J. Kell, "Development of a slender continuum robotic system for on-wing inspection/repair of gas turbine engines", *Robotics and Computer-Integrated Manufacturing*, Vol. 44, pp. 218–229, apr 2017.

15. Burgner-Kahrs, J., D. C. Rucker and H. Choset, "Continuum Robots for Medical Applications: A Survey", *IEEE Transactions on Robotics*, Vol. 31, No. 6, pp. 1261–1280, dec 2015.

16. Abidi, H., G. Gerboni, M. Brancadoro, J. Fras, A. Diodato, M. Cianchetti, H. Wurdemann, K. Althoefer and A. Menciassi, "Highly dexterous 2-module soft robot for

intra-organ navigation in minimally invasive surgery", *The International Journal of Medical Robotics and Computer Assisted Surgery*, Vol. 14, No. 1, p. e1875, feb 2018.

17. Wolf, A., H. Brown, R. Casciola, A. Costa, M. Schwerin, E. Shamas and H. Choset, "A mobile hyper redundant mechanism for search and rescue tasks", *Proceedings 2003 IEEE/RSJ International Conference on Intelligent Robots and Systems (IROS 2003) (Cat. No.03CH37453)*, Vol. 3, pp. 2889–2895, IEEE, 2003.

18. Mehling, J., M. Diftler, M. Chu and M. Valvo, "A Minimally Invasive Tendril Robot for In-Space Inspection", *The First IEEE/RAS-EMBS International Conference on Biomedical Robotics and Biomechatronics, 2006. BioRob 2006.*, pp. 690–695, IEEE, 2006.

19. Trivedi, D., C. D. Rahn, W. M. Kier and I. D. Walker, "Soft robotics: Biological inspiration, state of the art, and future research", *Applied Bionics and Biomechanics*, Vol. 5, No. 3, pp. 99–117, dec 2008.

20. Robinson, G. and J. Davies, "Continuum robots - a state of the art", *Proceedings 1999 IEEE International Conference on Robotics and Automation (Cat. No.99CH36288C)*, Vol. 4, pp. 2849–2854, IEEE, 1999.

21. Renda, F., M. Cianchetti, M. Giorelli, A. Arienti and C. Laschi, "A 3D steady-state model of a tendon-driven continuum soft manipulator inspired by the octopus arm", *Bioinspiration & Biomimetics*, Vol. 7, No. 2, p. 025006, jun 2012.

22. Rus, D. and M. T. Tolley, "Design, fabrication and control of soft robots", *Nature*, Vol. 521, No. 7553, pp. 467–475, may 2015.

23. Daerden, F., D. Lefeber, B. Verrelst and R. Van Ham, "Pleated pneumatic artificial muscles: actuators for automation and robotics", *2001 IEEE/ASME International Conference on Advanced Intelligent Mechatronics. Proceedings (Cat. No.01TH8556)*, Vol. 2, pp. 738–743, IEEE, 2001.

24. Greer, J. D., T. K. Morimoto, A. M. Okamura and E. W. Hawkes, "Series pneumatic artificial muscles (sPAMs) and application to a soft continuum robot", *Proceedings - IEEE International Conference on Robotics and Automation*, pp. 5503–5510, 2017.

25. Camarillo, D., C. Carlson and J. Salisbury, "Configuration Tracking for Continuum Manipulators With Coupled Tendon Drive", *IEEE Transactions on Robotics*, Vol. 25, No. 4, pp. 798–808, aug 2009.

26. Burdick, J. W., "A Modal Approach to Hyper-Redundant Manipulator Kinematics", *IEEE Transactions on Robotics and Automation*, Vol. 10, No. 3, pp. 343–354, jun 1994.

27. Webster, R. J. and B. A. Jones, "Design and Kinematic Modeling of Constant Curvature Continuum Robots: A Review", *The International Journal of Robotics Research*, Vol. 29, No. 13, pp. 1661–1683, nov 2010.

28. Marchese, A. D. and D. Rus, "Design, kinematics, and control of a soft spatial fluidic elastomer manipulator", *The International Journal of Robotics Research*, Vol. 35, No. 7, pp. 840–869, 2016.

29. Della Santina, C., R. K. Katzschmann, A. Biechi and D. Rus, "Dynamic control of soft robots interacting with the environment", *2018 IEEE International Conference on Soft Robotics (RoboSoft)*, pp. 46–53, IEEE, apr 2018.

30. Hannan, M. W. and I. D. Walker, "Kinematics and the Implementation of an Elephant's Trunk Manipulator and Other Continuum Style Robots", *Journal of Robotic Systems*, Vol. 20, No. 2, pp. 45–63, feb 2003.

31. Jones, B. and I. Walker, "Kinematics for multisection continuum robots", *IEEE Transactions on Robotics*, Vol. 22, No. 1, pp. 43–55, feb 2006.

32. Yip, M. C. and D. B. Camarillo, "Model-Less Hybrid Position/Force Control:

A Minimalist Approach for Continuum Manipulators in Unknown, Constrained Environments", *IEEE Robotics and Automation Letters*, Vol. 1, No. 2, pp. 844–851, jul 2016.

33. Giorelli, M., F. Renda, M. Calisti, A. Arienti, G. Ferri and C. Laschi, "Learning the inverse kinetics of an octopus-like manipulator in three-dimensional space", *Bioinspiration & Biomimetics*, Vol. 10, No. 3, p. 035006, may 2015.

34. Largilliere, F., V. Verona, E. Coevoet, M. Sanz-Lopez, J. Dequidt and C. Duriez, "Real-time control of soft-robots using asynchronous finite element modeling", *2015 IEEE International Conference on Robotics and Automation (ICRA)*, pp. 2550–2555, IEEE, may 2015.

35. Thuruthel, T. G., E. Falotico, F. Renda and C. Laschi, "Learning dynamic models for open loop predictive control of soft robotic manipulators", *Bioinspiration & Biomimetics*, Vol. 12, No. 6, p. 066003, oct 2017.

36. Qi, P., C. Liu, A. Ataka, H. K. Lam and K. Althoefer, "Kinematic Control of Continuum Manipulators Using a Fuzzy-Model-Based Approach", *IEEE Transactions on Industrial Electronics*, Vol. 63, No. 8, pp. 5022–5035, aug 2016.

37. Mahl, T., A. Hildebrandt and O. Sawodny, "A Variable Curvature Continuum Kinematics for Kinematic Control of the Bionic Handling Assistant", *IEEE Transactions on Robotics*, Vol. 30, No. 4, pp. 935–949, aug 2014.

38. Melingui, A., O. Lakhal, B. Daachi, J. B. Mbede and R. Merzouki, "Adaptive Neural Network Control of a Compact Bionic Handling Arm", *IEEE/ASME Transactions on Mechatronics*, Vol. 20, No. 6, pp. 2862–2875, dec 2015.

39. Lakhal, O., A. Melingui and R. Merzouki, "Hybrid Approach for Modeling and Solving of Kinematics of a Compact Bionic Handling Assistant Manipulator", *IEEE/ASME Transactions on Mechatronics*, Vol. 21, No. 3, pp. 1326–1335, jun 2016.

40. Kapadia, A. D., K. E. Fry and I. D. Walker, "Empirical investigation of closed-loop control of extensible continuum manipulators", *2014 IEEE/RSJ International Conference on Intelligent Robots and Systems*, pp. 329–335, IEEE, sep 2014.

41. Rolf, M. and J. J. Steil, "Efficient exploratory learning of inverse kinematics on a bionic elephant trunk", *IEEE Transactions on Neural Networks and Learning Systems*, Vol. 25, No. 6, pp. 1147–1160, jun 2014.

42. Reinhart, R., Z. Shareef, J. Steil, R. F. Reinhart, Z. Shareef and J. J. Steil, "Hybrid Analytical and Data-Driven Modeling for Feed-Forward Robot Control †", *Sensors*, Vol. 17, No. 2, p. 311, feb 2017.

43. Falkenhahn, V., A. Hildebrandt, R. Neumann and O. Sawodny, "Dynamic Control of the Bionic Handling Assistant", *IEEE/ASME Transactions on Mechatronics*, Vol. 22, No. 1, pp. 6–17, feb 2017.

44. Giorelli, M., F. Renda, G. Ferri and C. Laschi, "A feed-forward neural network learning the inverse kinetics of a soft cable-driven manipulator moving in three-dimensional space", *IEEE International Conference on Intelligent Robots and Systems*, pp. 5033–5039, IEEE, nov 2013.

45. Rolf, M., J. J. Steil and M. Gienger, "Online Goal Babbling for rapid bootstrapping of inverse models in high dimensions", *2011 IEEE International Conference on Development and Learning (ICDL)*, pp. 1–8, IEEE, aug 2011.

46. Baydere, B. A., S. K. Talas and E. Samur, "A novel highly-extensible 2-DOF pneumatic actuator for soft robotic applications", *Sensors and Actuators A: Physical*, Vol. 281, pp. 84–94, 2018.

47. Talas, S. K., B. A. Baydere, T. Altinsoy, C. Tutcu and E. Samur, "Design and Development of a Growing Pneumatic Soft Robot", *Soft Robotics*, In Review, 2019.

48. Tutcu, C., B. A. Baydere, S. K. Talas and E. Samur, "Quasi-static Modeling of a Novel Growing Soft-Continuum Robot", *International Journal of Robotics Research*, In Review, 2019.

49. Sadeghi, A., A. Mondini and B. Mazzolai, "Toward Self-Growing Soft Robots Inspired by Plant Roots and Based on Additive Manufacturing Technologies", *Soft Robotics*, Vol. 4, No. 3, pp. 211–223, sep 2017.

50. Hawkes, E. W., L. H. Blumenschein, J. D. Greer and A. M. Okamura, "A soft robot that navigates its environment through growth", *Science Robotics*, Vol. 2, No. 8, p. eaan3028, jul 2017.

51. Altinsoy, T., B. A. Baydere, S. K. Talas, O. M. Erkan, C. Tutcu and E. Samur, "Design of an Extensible Colonosopy Robot", *Hamlyn Symposium on Medical Robotics*, pp. 25–26, 2018.

52. Langer, M., E. Amanov and J. Burgner-Kahrs, "Stiffening Sheaths for Continuum Robots", *Soft Robotics*, Vol. 5, No. 3, pp. 291–303, jun 2018.

APPENDIX A: DATASHEETS

HIGH TORQUE HYBRID STEPPING MOTOR SPECIFICATIONS

General specifications		Electrical specifications	
Step Angle (°)	1.8	Rated Voltage (V)	4.56
Temperature Rise (℃)	80 Max (rated current. 2 phase on)	Rated Current (A)	0.67
Ambient Temperature (℃)	-20~+50	Resistance Per Phase (±10% Ω)	6.8 (25℃)
Number of Phase	2	Inductance Per Phase (±20% mH)	4.9
Insulation Resistance (MΩ)	100 Min (500VDC)	Holding Torque (N.cm)	9.5
Insulation Class	Class B	Detent Torque (N.cm)	
Max.radial force (N)	28 (20mm from the flange)	Rotor Torque ($g.cm^2$)	9
Max.axial force (N)	10	Weight (Kg)	0.12

● Wiring Diagram :

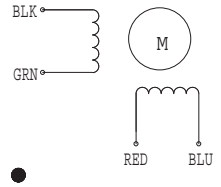

SY28STH45-0674A Pull out torque curve:
VOLTAGE: 24VDC, CONSTANT CURRENT:0.67A,HALF STEP

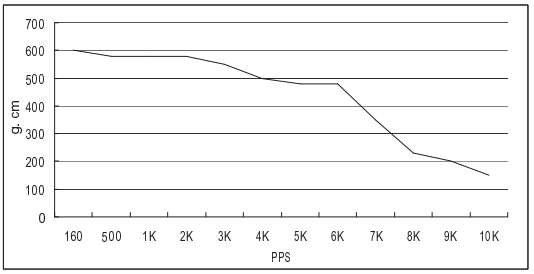

●

Dimensions:
(unit=mm)

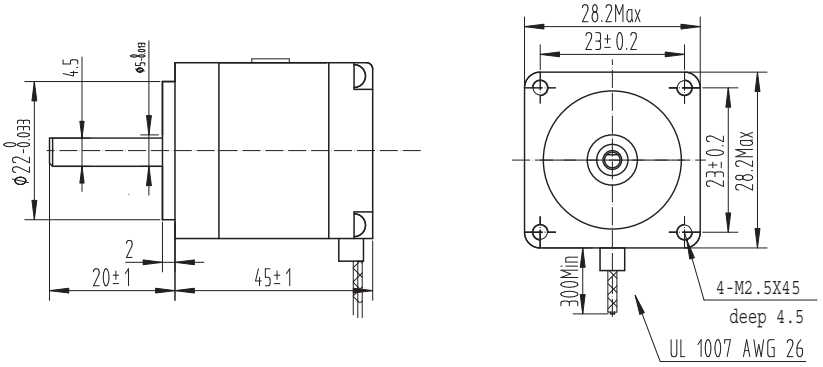

REV	REVISIONS	DESCRIPTION	BY	DATE	SY28STH45-0674A	TECHNICAL CONDITIONS
DRAW	kongxiangzhen 2012.05.12				CHANGZHOU SONGYANG MACHINERY & ELECTRONICS NEW TECHNIC INSTITUTE	020045012
CHECK						
APPROVE						

Figure A.1. Stepper motor datasheet.

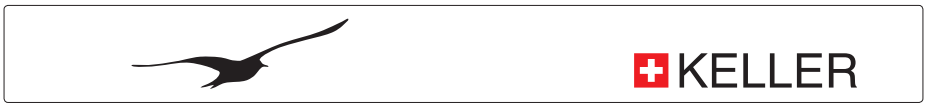

Specifications

Pressure Ranges (all intermediate ranges possible)		
PR-21 Y	2…30	bar FS
PAA-21 Y / PA-21 Y	2…1000*	bar FS
Overpressure	2 x pressure range, max. 1100 bar	

PAA: Absolute. Zero at vacuum PA: Sealed Gauge. Zero at 1000 mbar abs. PR: Vented Gauge. Zero at atmospheric pressure * Measuring range > 600 bar only suited for static applications

Accuracy			
Linearity (best fitted straight line) [1]		typ. ±0,25 %FS	max. ±0,5 %FS
Total Error Band [2]	0...50 °C	max. ±1,0 %FS	
	-10...80 °C	max. ±1,5 %FS	

[1] including Hysteresis + Repeatability [2] Linearity + Hysteresis + Repeatability + Temp. Coeff. + Zero + Span Tolerance

Storage-/Operating Temperature		-40…100 °C
Stability	PR-Version	max. ±0,5 %FS
	PAA/PA-Version	max. ±0,3 %FS

Type	2-Wire	3-Wire	3-Wire
Signal Output	**4...20 mA**	**0...10 V**	**0,5…4,5 V**
Limitation Signal Output	3,2...22,3 mA	-1,2...11,2 V	0,1...4,9 V
Supply	8...32 VDC	13...32 VDC	8...32 VDC
Load Resistance	< (U-8 V) / 0,025 A	> 5 kΩ	> 5 kΩ
Limiting Frequency	2 kHz	2 kHz	2 kHz
Power Consumption		max. 5 mA	max. 4 mA

Electrical Connection	- Plug: M12 (4-pole), Packard, mPm - Cable
Pressure Connection	G1/4" male, G1/8" male, 7/16"-20 UNF male and female
Response Time (Supply ON)	(0…99 %) < 5 ms
Isolation	> 10 MΩ at 300 VDC
EMC	EN 61000-6-2: 2005 / EN 61000-6-3: 2007 / EN 61326-2-3: 2006
Dead Volume Change	< 0,1 mm^3
Material in Media Contact	- Stainless Steel AISI 316L (1.4404/1.4435) - Viton® Seal external (-20…200 °C, no internal seals)
Protection Class	M12-/Packard-Plug: IP67 (with corresponding mating plug) mPm-Plug: IP65 (with corresponding mating plug) Cable: IP54
Weight	≈ 38 g (G1/8") ≈ 50 g (G1/4")
Endurance	> 10 million cycles, 0…100 %FS at 25 °C
Oil Filling	Silicone oil

Options

Temperature Range	Other temperature ranges on request. Maximal range: -40…+120 °C
Oil Filling	Fluorocarbon oil (O_2-compatible), olive-oil, lowest temperature oil (-55 °C)
Pressure Connection, Electr.ical Connection	Others on request

KELLER AG für Druckmesstechnik
CH-8404 Winterthur
+41 52 235 25 25
info@keller-druck.com

KELLER Ges. für Druckmesstechnik mbH
D-79798 Jestetten
+49 7745 9214 0
eurocenter@keller-druck.com

Edition 06/2016
Subject to alterations
Companies approved to ISO 9001
www.keller-druck.com

Figure A.2. Pressure transducer datasheet.

FAIRCHILD
SEMICONDUCTOR TM

BD135/137/139

Medium Power Linear and Switching Applications

- Complement to BD136, BD138 and BD140 respectively

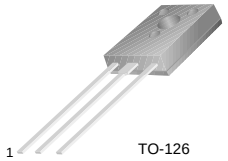

TO-126

1. Emitter 2.Collector 3.Base

NPN Epitaxial Silicon Transistor

Absolute Maximum Ratings T_C=25°C unless otherwise noted

Symbol	Parameter	Value	Units
V_{CBO}	Collector-Base Voltage : BD135	45	V
	: BD137	60	V
	: BD139	80	V
V_{CEO}	Collector-Emitter Voltage : BD135	45	V
	: BD137	60	V
	: BD139	80	V
V_{EBO}	Emitter-Base Voltage	5	V
I_C	Collector Current (DC)	1.5	A
I_{CP}	Collector Current (Pulse)	3.0	A
I_B	Base Current	0.5	A
P_C	Collector Dissipation (T_C=25°C)	12.5	W
P_C	Collector Dissipation (T_a=25°C)	1.25	W
T_J	Junction Temperature	150	°C
T_{STG}	Storage Temperature	- 55 ~ 150	°C

Electrical Characteristics T_C=25°C unless otherwise noted

Symbol	Parameter	Test Condition	Min.	Typ.	Max.	Units
V_{CEO}(sus)	Collector-Emitter Sustaining Voltage					
	: BD135	I_C = 30mA, I_B = 0	45			V
	: BD137		60			V
	: BD139		80			V
I_{CBO}	Collector Cut-off Current	V_{CB} = 30V, I_E = 0			0.1	µA
I_{EBO}	Emitter Cut-off Current	V_{EB} = 5V, I_C = 0			10	µA
h_{FE1}	DC Current Gain : ALL DEVICE	V_{CE} = 2V, I_C = 5mA	25			
h_{FE2}	: ALL DEVICE	V_{CE} = 2V, I_C = 0.5A	25			
h_{FE3}	: BD135	V_{CE} = 2V, I_C = 150mA	40		250	
	: BD137, BD139		40		160	
V_{CE}(sat)	Collector-Emitter Saturation Voltage	I_C = 500mA, I_B = 50mA			0.5	V
V_{BE}(on)	Base-Emitter ON Voltage	V_{CE} = 2V, I_C = 0.5A			1	V

h_{FE} Classification

Classification	6	10	16
h_{FE3}	40 ~ 100	63 ~ 160	100 ~ 250

Rev. A, February 2000

Figure A.3. Transistor datasheet.

THREE WAY NORMALLY CLOSED DIRECT ACTING SOLENOID VALVE

C01

GENERAL DESCRIPTION / APPLICATIONS

Three way direct acting solenoid valve with spring return, normally close.

Suitable for gaseous and liquid media compatible with the used material (body/seals), vacuum.

Forged brass body.
Brass guide tube.
Stainless steel internal parts.
Stainless steel springs.

Solenoid can be rotated 360°.

Valve will operate in any position.

DIMENSIONS mm

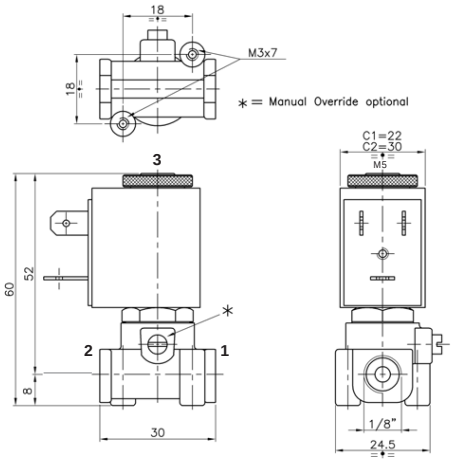

ELETTRICAL INFORMATIONS

Continuous duty glass-reinforced nylon mouldedcoil with electrical connection suitable for DIN-43650 plug (2 poles+ground) or faston wire terminal . Two cables available on request.

Coil type:	C1
Insulation class:	F (155°C), H (180°C) on request.
Winding wire class:	H (180°C)
Protection class:	Waterproof IP-65 (norme EN60529) when properly plug connetted when DIN-43650 plug.
Duty:	Continuous (S.I.) 100% ED
Power consumption:	Alternate Current 8VA (inrush 12VA) Direct Current 5,5W
Voltage tollerance:	a.c. +10% ÷ -15%, d.c. +10% ÷ -5%
Elettrical Insulation:	>500 MOhm
Dielectrical Strenght:	>2000 V/1'
Standard voltage:	d.c. 12, 24 Volt a.c. 24, 110, 230 Volt (50/60 Hz) other voltages available on request.

OPERATION

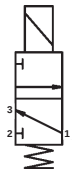

Normally closed

In :	2
Out :	1
Vent :	3
Coil de-energised :	Input 2 closed From 1 to vent 3
Coil energised :	From 2 to 1 Vent 3 closed

SPECIFICATIONS AND AVAILABLE OPTIONS

MODEL a b	c d	e f	ORIFICE mm	BODY RATING MAX.	PRESSURES IN BAR MIN. / MAX. DIFFERENZIAL PRESSURES MIN.	MAX. AC~	MAX. DC=	Flow factor kv (liters/min.')	Weight Kg
C 01	B	12	1,2 (1,2)	15	0	15	15	0,65	0,14
C 01	B	15	1,5 (1,5)	10	0	10	10	1	0,14
C 01	B	20	2,0 (1,9)	6	0	6	6	1,5	0,14

a Construction	b Valve type	c Port size G	d Seals material	e Body material	f Optional feature
A AC C DC	C 3 way	B 2 and 1 : 1/8" GAS 3 : M5	B NBR V VITON E EPDM	T Brass N Nichel-plated brass	M Manual override SG Clean for oxigene I Stainless steel guide tube

FG line srl - Via dell'Industria, 32/36 - 24126 Bergamo (BG) - Italy Tel. +39 035 322441 - Fax +39 035 322439 - Internet: www.fgline.it e-mail: fgline@fgline.it

Figure A.4. Solenoid valve datasheet.

Allegro MicroSystems, Inc.

A4983

DMOS Microstepping Driver with Translator

Features and Benefits

- Low $R_{DS(ON)}$ outputs
- Automatic current decay mode detection/selection
- Mixed and Slow current decay modes
- Synchronous rectification for low power dissipation
- Internal UVLO
- Crossover-current protection
- 3.3 and 5 V compatible logic supply
- Very thin profile QFN package
- Thermal shutdown circuitry

Package: 28-pin QFN (suffix ET)

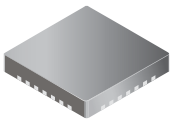

Approximate size 

Description

The A4983 is a complete microstepping motor driver with built-in translator for easy operation. It is designed to operate bipolar stepper motors in full-, half-, quarter-, eighth, and sixteenth-step modes, with an output drive capacity of up to 35 V and ±2 A. The A4983 includes a fixed off-time current regulator which has the ability to operate in Slow or Mixed decay modes.

The translator is the key to the easy implementation of the A4983. Simply inputting one pulse on the STEP input drives the motor one microstep. There are no phase sequence tables, high frequency control lines, or complex interfaces to program. The A4983 interface is an ideal fit for applications where a complex microprocessor is unavailable or is overburdened.

The chopping control in the A4983 automatically selects the current decay mode (Slow or Mixed). When a signal occurs at the STEP input pin, the A4983 determines if that step results in a higher or lower current in each of the motor phases. If the change is to a higher current, then the decay mode is set to Slow decay. If the change is to a lower current, then the current decay is set to Mixed (set initially to a fast decay for a period amounting to 31.25% of the fixed off-time, then to a

Continued on the next page…

Typical Application Diagram

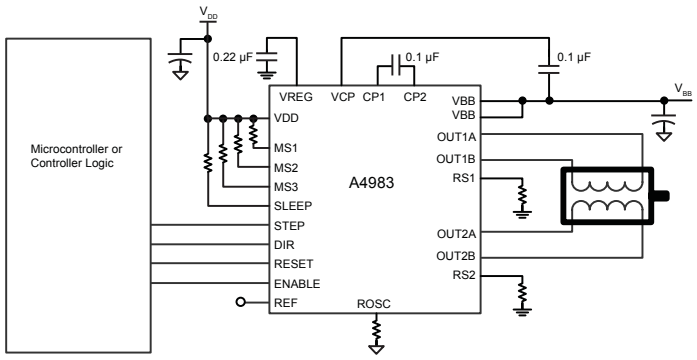

Figure A.5. Motor driver datasheet.

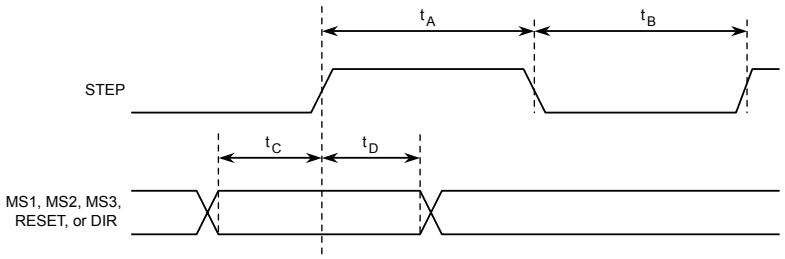

Time Duration	Symbol	Typ.	Unit
STEP minimum, HIGH pulse width	t_A	1	µs
STEP minimum, LOW pulse width	t_B	1	µs
Setup time, input change to STEP	t_C	200	ns
Hold time, input change to STEP	t_D	200	ns

Figure 1. Logic Interface Timing Diagram

Table 1. Microstep Resolution Truth Table

MS1	MS2	MS3	Microstep Resolution	Excitation Mode
L	L	L	Full Step	2 Phase
H	L	L	Half Step	1-2 Phase
L	H	L	Quarter Step	W1-2 Phase
H	H	L	Eighth Step	2W1-2 Phase
H	H	H	Sixteenth Step	4W1-2 Phase

Figure A.6. Motor driver datasheet cont.

DATASHEET

NI 9403

32 DIO, 5 V/TTL, Bidirectional, 7 µs

- 5 V/TTL, sinking/sourcing digital I/O
- Bidirectional, configurable by line with shift-on-the-fly capability
- 60 VDC, CAT I isolation
- Industry-standard 37-pin DSUB connector
- -40 °C to 70 °C operating, 5 g vibration, 50 g shock

The NI 9403 is a 32-channel, 7 µs bidirectional digital I/O module for any NI CompactDAQ or CompactRIO chassis. You can configure the direction of each digital line on the NI 9403 for input or output. Each channel is compatible with 5 V/TTL signals and features 60 VDC, CAT I isolation. The NI 9403 also features ±30 V overvoltage protection and can source up to 2 mA output current per channel.

In an NI CompactDAQ chassis, you can use the NI 9403 as only a static (software-timed) digital I/O module. Due to the serial transfer of data, you cannot use these modules to route timing or triggering signals. With the NI 9403 in a CompactRIO chassis, you can use LabVIEW FPGA to program the NI 9403 for implementing custom counter/timers, pulse generation, and much more.

C SERIES DIGITAL INPUT/OUTPUT MODULE COMPARISON

Product Name	Signal Levels	Channels	Update Rate	Direction	Connectivity	Isolation Continuous
NI 9381	LVTTL	4	1 µs	Bidirectional	DSUB	None
NI 9401	5 V/TTL	8	100 ns	Bidirectional	DSUB	60 VDC Ch-Earth
NI 9402	LVTTL	4	55 ns	Bidirectional	BNC	None
NI 9403	5 V/TTL	32	7 µs	Bidirectional	DSUB	60 VDC Ch-Earth

NATIONAL INSTRUMENTS

Figure A.7. NI 9403 datasheet.

DATASHEET

NI 9203 Datasheet

8-Channel, ±20 mA, 16-Bit Analog Input Module

- 8 channels, 200 kS/s current input
- ±20 mA, 0 mA to 20 mA programmable input ranges; 16-bit resolution
- NIST-traceable calibration
- Screw-terminal or spring-terminal connectivity
- 250 V_{rms}, CAT II bank isolation
- -40 °C to 70 °C operating range, 5 g vibration, 50 g shock

The NI 9203 is a C Series DAQ module with 8 analog current input channels for high-performance control and monitoring applications. It features programmable input ranges of ±20 mA or 0 mA to 20 mA, 16-bit resolution, and a 200 kS/s maximum sampling rate. To protect against signal transients, the NI 9203 includes a channel-to-earth ground double-isolation barrier (250 V_{rms} isolation) for safety and noise immunity.

Input Circuitry

The input signals are buffered, conditioned, and sampled by a single 16-bit ADC. The module protects each channel from overvoltages. Refer to the Specifications section for information about overvoltage protection.

Figure 1. Input Circuitry on the NI 9203

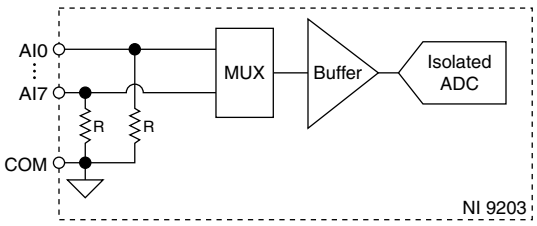

Specifications

The following specifications are typical for the range -40 °C to 70 °C unless otherwise noted. All voltages are relative to COM unless otherwise noted.

Figure A.8. NI 9203 datasheet.

APPENDIX B: LABVIEW CODES

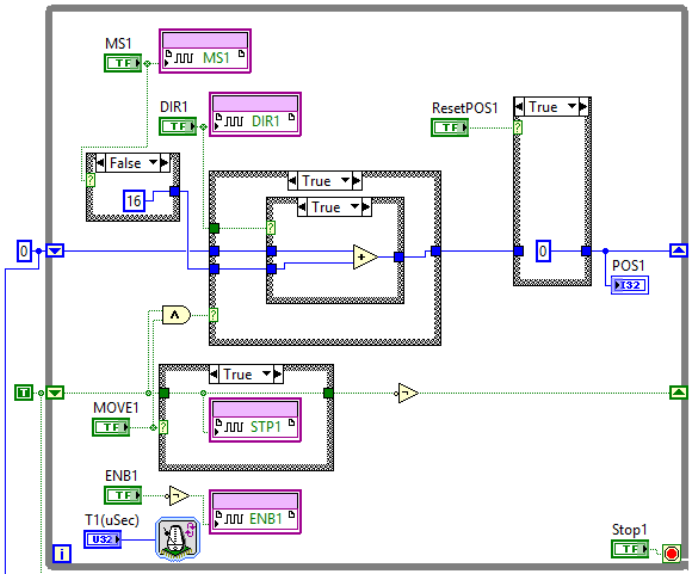

Figure B.1. FPGA control loop of a stepper motor.

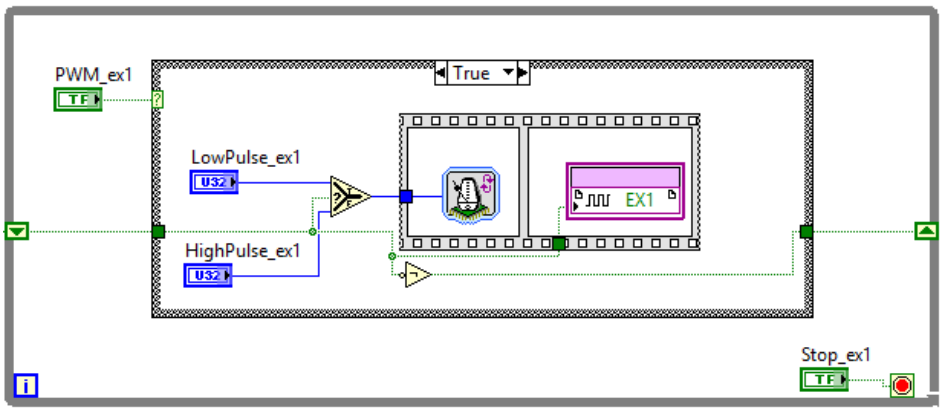

Figure B.2. FPGA control loop of an exhaust valve.

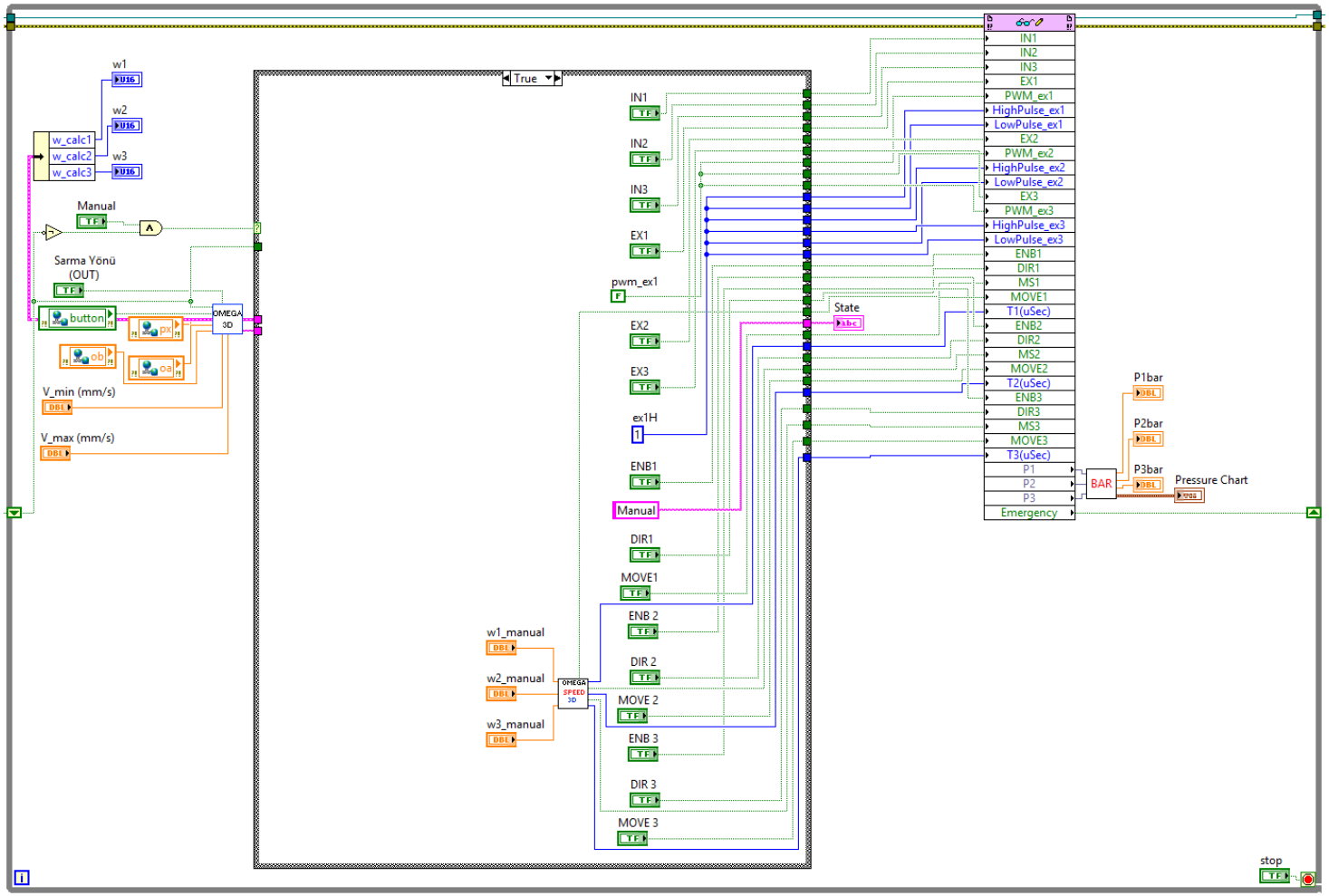

Figure B.3. Main RTOS control loop.

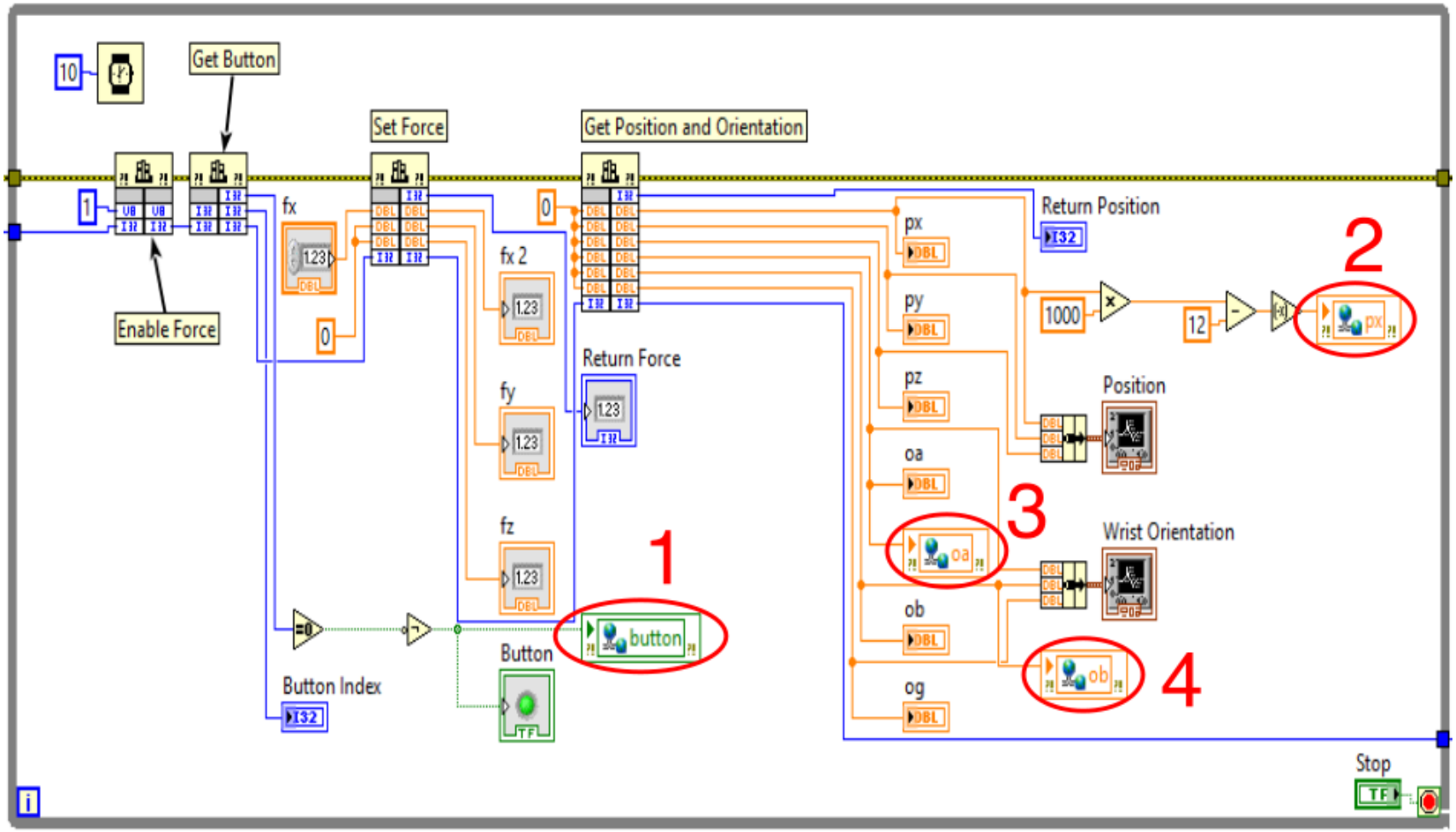

Figure B.4. LabView code to read data from omega.6. Labeled data which are (1) button, (2) p_x, (3) α, (4) β, are sent to the teleoperation controller.

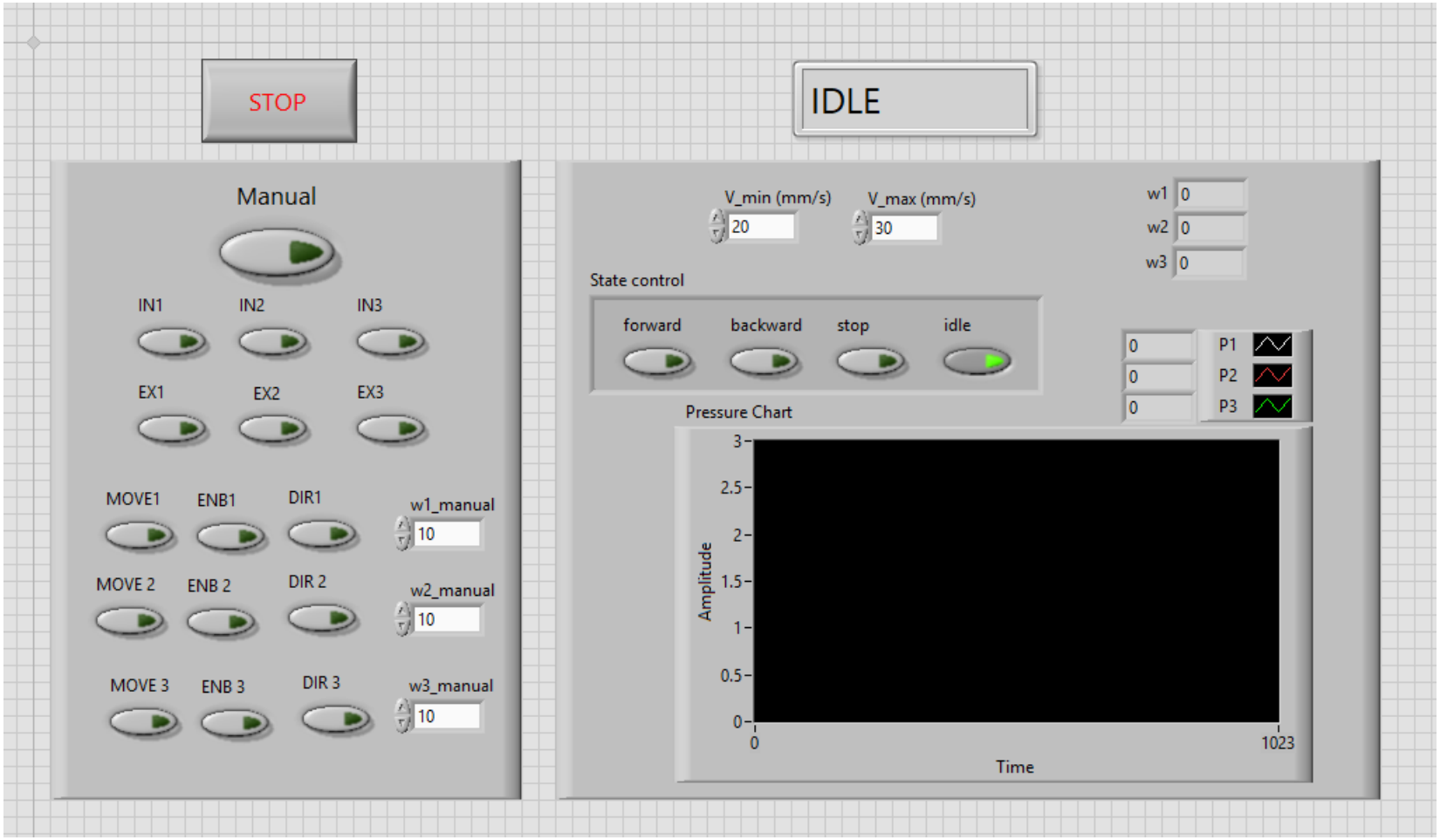

Figure B.5. Graphical user interface of the main control code.

APPENDIX C: MATHSCRIPT CODES

C.1. Teleoperation controller algorithm LabView MathScript code

```
states={'Emergency Stop','Forward','Backward','Stop','Idle'};
if emergency==true
state=states{1};
else
if button==true
if px>10
state=states{2};
elseif px<-10
state=states{3};
elseif px<10 && px>-10
state=states{4};
end
else
state=states{5};
end
end

if oa>60
oa=60;
elseif oa<-60
oa=-60;
end
if ob<0
ob=0;
elseif ob>70
ob=70;
```

```
end

alpha=oa*10/6;
beta=(ob-35)*10/3.5;

r=100;

r_ab=sqrt(alpha^2+beta^2);

if r_ab>r
Alpha=r*alpha/r_ab;
Beta=r*beta/r_ab;
r_ab=r;
else
Alpha=alpha;
Beta=beta;
end

%Direction regions
if r_ab<45
dir_reg=0;
else
if Beta>=Alpha*tan(pi/3) && Beta>=-Alpha*tan(pi/3)
dir_reg=1;
elseif Beta<Alpha*tan(pi/3) && Beta>0
dir_reg=12;
elseif Beta<=0 && Beta>=-Alpha*tan(pi/3)
dir_reg=2;
elseif Beta<Alpha*tan(pi/3) && Beta<-Alpha*tan(pi/3)
dir_reg=23;
elseif Beta>=Alpha*tan(pi/3) && Beta<=0
```

```
dir_reg=3;
elseif Beta>0 && Beta<-Alpha*tan(pi/3)
dir_reg=31;
end
end

r_sp=11.5; %mm spool radius
w_max=V_max/r_sp*60/pi;
w_min=V_min/r_sp*60/pi;

w=(w_max-w_min)*(abs(px)-10)/50+w_min;
w_slow=-0.5*w/85*(r_ab-15)+w

if dir_reg==0
w1=w;
w2=w;
w3=w;
elseif dir_reg==1
w1=w_slow;
w2=w;
w3=w;
elseif dir_reg==12
w1=w_slow;
w2=w_slow;
w3=w;
elseif dir_reg==2
w1=w;
w2=w_slow;
w3=w;
elseif dir_reg==23
w1=w;
```

```
w2=w_slow;
w3=w_slow;
elseif dir_reg==3
w1=w;
w2=w;
w3=w_slow;
elseif dir_reg==31
w1=w_slow;
w2=w;
w3=w_slow;
end

w_calc1=w1;
w_calc2=w2;
w_calc3=w3;

if strcmp(state,states{4})==true || strcmp(state,states{5})==true
w1=0;
w2=0;
w3=0;
end

%Motor 1
if w1>0
MOVE1=true;
if w1>195
MS1=false;
T1=150000/w1;
else
MS1=true;
T1=150000/16/w1;
```

```
end
elseif w1==0
MOVE1=false;
T1=1;
MS1=true;
end

%Motor 2
if w2>0
MOVE2=true;
if w2>195
MS2=false;
T2=150000/w2;
else
MS2=true;
T2=150000/16/w2;
end
elseif w2==0
MOVE2=false;
T2=1;
MS2=true;
end

%Motor 3
if w3>0
MOVE3=true;
if w3>195
MS3=false;
T3=150000/w3;
else
MS3=true;
```

```
T3=150000/16/w3;
end
elseif w3==0
MOVE3=false;
T3=1;
MS3=true;
end

T=40; %pwm period milisecond
Dc=15; %duty cycle
Th=Dc*T/100;
Tl=T-Th;

if strcmp(state,states{1})==true
ENB=false;
DIR1=OUT;
DIR2=not(OUT);
DIR3=OUT;
PWM_ex=false;
EX=true;
IN=false;
elseif strcmp(state,states{2})==true
ENB=true;
DIR1=OUT;
DIR2=not(OUT);
DIR3=OUT;
PWM_ex=false;
EX=false;
IN=true;
elseif strcmp(state,states{3})==true
ENB=true;
```

```
DIR1=not(OUT);
DIR2=OUT;
DIR3=not(OUT);
PWM_ex=true;
EX=false;
IN=true;
elseif strcmp(state,states{4})==true
ENB=true;
DIR1=OUT;
DIR2=not(OUT);
DIR3=OUT;
PWM_ex=false;
EX=false;
IN=true;
elseif strcmp(state,states{5})==true
ENB=true;
DIR1=OUT;
DIR2=not(OUT);
DIR3=OUT;
PWM_ex=false;
EX=false;
IN=false;
end
```